ADVANCED ENERGY MATERIALS
www.advenergymat.de

Atomically dispersed Fe in a C_2N Based Catalyst as a Sulfur Host for Efficient Lithium–Sulfur Batteries

Zhifu Liang, Dawei Yang, Pengyi Tang, Chaoqi Zhang, Jordi Jacas Biendicho, Yi Zhang, Jordi Llorca, Xiang Wang, Junshan Li, Marc Heggen, Jeremy David, Rafal E. Dunin-Borkowski, Yingtang Zhou, Joan Ramon Morante, Andreu Cabot,* and Jordi Arbiol**

Lithium–sulfur batteries (LSBs) are considered to be one of the most promising next generation energy storage systems due to their high energy density and low material cost. However, there are still some challenges for the commercialization of LSBs, such as the sluggish redox reaction kinetics and the shuttle effect of lithium polysulfides (LiPS). Here a 2D layered organic material, C_2N, loaded with atomically dispersed iron as an effective sulfur host in LSBs is reported. X-ray absorption fine spectroscopy and density functional theory calculations prove the structure of the atomically dispersed Fe/C_2N catalyst. As a result, Fe/C_2N-based cathodes demonstrate significantly improved rate performance and long-term cycling stability. Fe/C_2N-based cathodes display initial capacities up to 1540 mAh g^{-1} at 0.1 C and 678.7 mAh g^{-1} at 5 C, while retaining 496.5 mAh g^{-1} after 2600 cycles at 3 C with a decay rate as low as 0.013% per cycle. Even at a high sulfur loading of 3 mg cm^{-2}, they deliver remarkable specific capacity retention of 587 mAh g^{-1} after 500 cycles at 1 C. This work provides a rational structural design strategy for the development of high-performance cathodes based on atomically dispersed catalysts for LSBs.

1. Introduction

Lithium–sulfur batteries (LSBs) are considered one of the main candidate technologies for next generation energy storage systems. The main advantages of LSBs are their high theoretical capacity (≈1675 mAh g^{-1}) and high energy density (≈2600 Wh kg^{-1}), which is about five times higher than that of lithium-ion batteries.[1–4] Besides, sulfur, the active cathode material, is highly abundant in the earth crust and it has a low cost and no major environmental, health, and safety issues.[5] While LSBs are extremely appealing, some serious drawbacks still impede their practical application. These drawbacks include the low electrical conductivity of sulfur and lithium sulfides, the sluggish Li–S reaction kinetics, the large volume changes during lithiation/delithiation and the shuttle effect of

Z. F. Liang, Dr. J. David, Prof. J. Arbiol
Catalan Institute of Nanoscience and Nanotechnology (ICN2)
CSIC and BIST
Campus UAB, Bellaterra, Catalonia, Barcelona 08193, Spain
E-mail: arbiol@icrea.cat

Z. F. Liang, D. W. Yang, C. Q. Zhang, Dr. J. Jacas Biendicho, X. Wang, Prof. J. R. Morante, Prof. A. Cabot
Catalonia Institute for Energy Research - IREC
Sant Adrià de Besòs
Catalonia, Barcelona 08930, Spain
E-mail: acabot@irec.cat

D. W. Yang, C. Q. Zhang, X. Wang, Prof. J. R. Morante
Department of Electronic and Biomedical Engineering
Universitat de Barcelona
Catalonia, Barcelona 08028, Spain

Dr. P. Y. Tang, Dr. M. Heggen, Prof. R. E. Dunin-Borkowski
Ernst Ruska-Centre for Microscopy and Spectroscopy with Electrons and Peter Grünberg Institute "Forschungszentrum Jülich GmbH"
Jülich 52425, Germany

Prof. Y. Zhang
School of Energy Sciences and Engineering
Nanjing Tech University
Nanjing, Jiangsu 211816, China

The ORCID identification number(s) for the author(s) of this article can be found under https://doi.org/10.1002/aenm.202003507.

Prof. J. Llorca
Institute of Energy Technologies
Department of Chemical Engineering and Barcelona Research Center in Multiscale Science and Engineering
Universitat Politècnica de Catalunya
EEBE
Catalonia, Barcelona 08019, Spain

Dr. J. Li
Institute of Fundamental and Frontier Sciences
University of Electronic Science and Technology of China
Chengdu 610054, China

Prof. Y. T. Zhou
Key Laboratory of Health Risk Factors for Seafood and Environment of Zhejiang Province
Institute of Innovation & Application
Zhejiang Ocean University
Zhoushan, Zhejiang 316022, China
E-mail: zhouyingtang@zjou.edu.cn

Prof. A. Cabot, Prof. J. Arbiol
ICREA
Pg. Lluís Companys 23, Catalonia, Barcelona 08010, Spain

DOI: 10.1002/aenm.202003507

soluble lithium polysulfide (LiPS) Li_2S_x ($3 < x \leq 8$). The latter has associated an irreversible loss of active material at the cathode and the corrosion of the lithium metal anode, overall resulting in a rapid capacity fading and a poor coulombic efficiency that greatly reduce the rate performance, cycling stability and lifespan of LSBs.[6,7]

An effective strategy to increase electrical conductivity and accommodate volume changes is the use of high surface area and high porosity carbon-based materials as sulfur hosts,[15] e.g., mesocarbon,[8] graphene,[9] porous carbon,[10] carbon nanotubes,[11] conducting polymers such as polyaniline[12] or covalent organic frameworks (COFs).[13,14] These porous materials also limit LiPS diffusion by hampering their transport, but they just weakly physically interact with LiPS, which is insufficient to inhibit the shuttle effect. To overcome this limitation, heteroatoms with stronger electronegativity, e.g., O, N, S, and P, have been introduced in carbon-based materials to improve their interaction with LiPS.[16–18] While several of these heteroatom-doped carbon-based sulfur hosts have demonstrated improved electrochemistry performance, this strategy is far from its optimization. The main difficulty toward optimizing these complex materials is the intricate characterization of the heteroatom dispersion, which translates in a very challenging control of the materials parameters during synthesis and an unreliable characterization of the electrochemical mechanisms and the structure-performance relationships.

Recently, 2D organic materials with a periodic porous structure, large surface area, and controllable chemical composition and functionality have been demonstrated as excellent sulfur hosts in LSBs.[19,20] On the other hand, single-atom catalysts (SACs) based on atomically dispersed metal atoms have demonstrated outstanding catalytic performances in several reactions, including Li–S redox reactions.[21–25] Besides maximizing the metal dispersion, the main advantage of SACs is their high surface energy, which allows decreasing the energy barrier of several catalytic processes.

C_2N, a 2D graphene-like layered organic material was synthesized for the first time in 2015 through a wet chemistry method by Beak and co-workers.[43] Since then, several C_2N-based materials have been developed for their application in electrocatalysis and batteries, e.g., Ru/C_2N for hydrogen evolution,[26,27] Fe/C_2N for oxygen reduction,[28] and C_2N for lithium-ion batteries.[29] In C_2N, pores are surrounded by six pyridine nitrogen atoms, which can be either coordinated with a metal atom or used themselves as traps for polysulfides and lithium ions, as predicted theoretically.[30] Using DFT calculations, Lin et al. further predicted that metal atoms embedded in C_2N as SACs could hinder the shuttle effect and accelerate the electrochemical conversion between sulfur and Li_2S.[31] Nevertheless, the extremely challenging preparation of C_2N-based catalysts containing an atomic metal distribution has so far prevented to experimentally corroborate these expectations.

Here, we report on the synthesis of atomically and uniformly dispersed iron on C_2N frameworks (Fe/C_2N). These new catalysts present several advantages as sulfur host in LSBs. First, C_2N frameworks show a high polarity and excellent electrical conductivity due to the abundance of pyrazine nitrogen and their planar 2D π-conjugated properties. Second, C_2N is a highly porous and high surface area framework, allowing the efficient transport of lithium ions and the effective absorption of polysulfide. Third, two iron atoms can be trapped in each hole, coordinating to the neighbor nitrogen atoms, to act as active sites for the conversion reaction of polysulfide during the charging and discharging processes. For all these reasons, the produced Fe/C_2N based catalysts were tested as sulfur cathode host materials in LSBs.

2. Results and Discussion

Fe/C_2N composites were synthesized as illustrated in **Figure 1**a. First, C_2N was prepared via a polycondensation reaction and a subsequent annealing process.[32,33] Next, Fe/C_2N was obtained by a pyrolysis treatment of a mixture of C_2N and iron (III) nitrate. Fe/C_2N displayed a granule-type morphology, as observed by scanning electron microscopy (SEM) (Figure S1a, Supporting Information). High resolution transmission electron microscopy (HRTEM) analysis showed no iron nanoparticles attached or near the Fe/C_2N structure (Figure S1b, Supporting Information); and the corresponding fast Fourier transform (FFT) or power spectra of the Fe/C_2N structure indicated C_2N to present an amorphous or a low crystallinity structure. As shown in Figure 1b and the enlarged image in Figure 1c, isolated Fe atoms (labeled in yellow) and double iron atom sites (labeled in red) which showed a low crystallinity structure were clearly observed using high angle annular dark field (HAADF)-aberration corrected (AC) scanning transmission electron microscopy (STEM), further these STEM images in Figure S2 (Supporting Information) supported the homogenous distribution of iron. Energy-dispersive X-ray spectroscopy (EDS) elemental mapping (Figure 1d and Figure S1c: Supporting Information) showed that Fe, C, N, and O are uniformly distributed. It is worth noting that the presence of oxygen was mainly coming from the solution used for the TEM sample preparation and the fact that the C_2N structure present high polarity holes with high affinity for trapping oxygen and moisture. To confirm this low crystallinity structure and to discard any electron beam damage during HRTEM characterization, Fe/C_2N was further analyzed by powder X-ray diffraction (XRD, Figure S3a, Supporting Information). XRD confirmed the C_2N to present a low crystallinity, with a main broad and weak diffraction peak at about 26.5°. This peak, common for graphene-like materials, corresponded to a 0.33 nm d-spacing of the (002) crystal plane of the C_2N layered structure. It is important to highlight that no peak corresponding to an iron-based lattice structure was observed. The latter experimental evidence confirmed the absence of Fe-related nanoparticles or clusters, thus pointing toward an atomic dispersion of Fe which is consistent with SEM-EDX, HRTEM, and HAADF-AC-STEM results.

Thermogravimetric analysis (TGA) showed the weight of Fe/C_2N samples to decrease to 0.9% when heating them to 700 °C under air (Figure S3b, Supporting Information). The remaining 0.9% mass was associated to Fe_2O_3, which is consistent with a 0.67 wt% iron content in the initial Fe/C_2N.

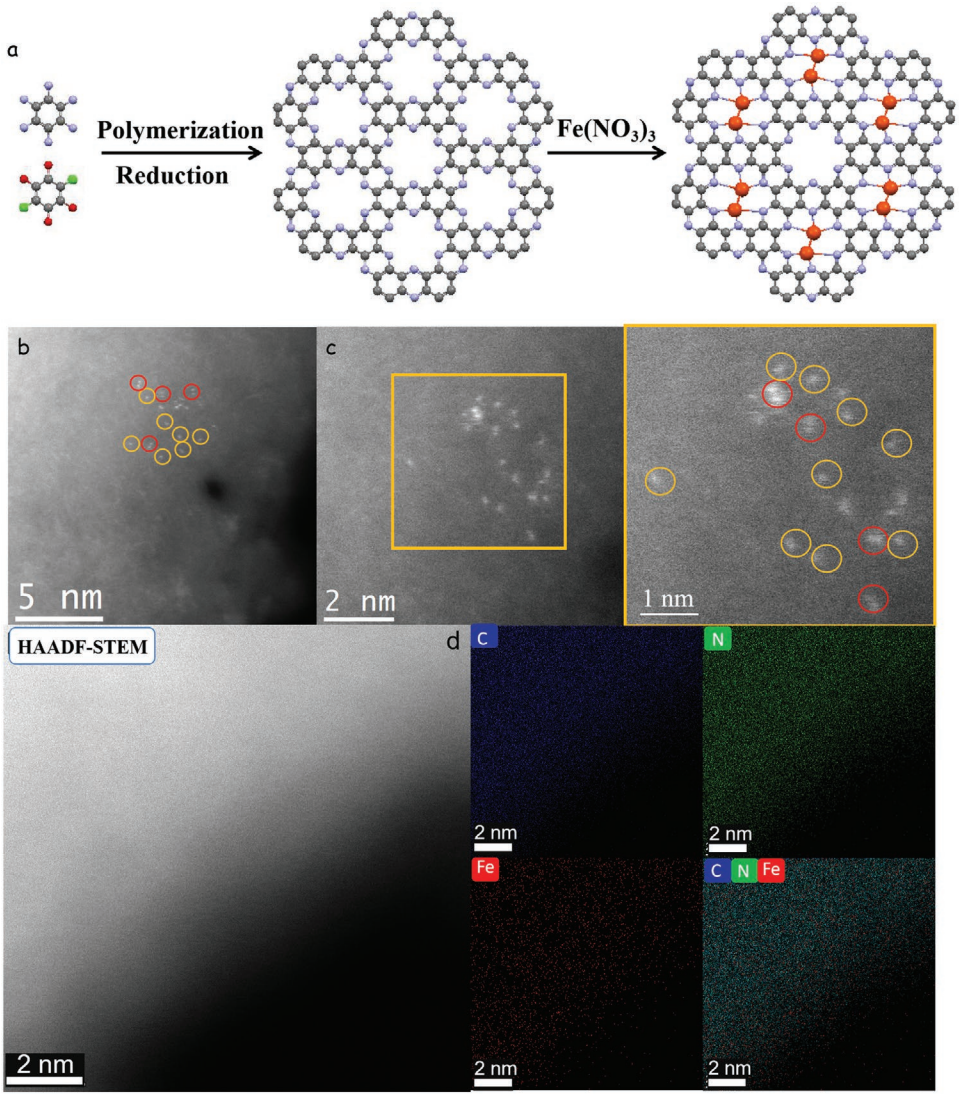

Figure 1. a) Schematic illustration of the synthesis route for the Fe/C_2N 2D layered material (blue = nitrogen, gray = carbon, red = oxygen, green = chlorine, and orange = iron). b,c) HAADF-STEM images of a Fe/C_2N catalyst showing the presence of atomically dispersed iron species: double iron clusters are circled in red and single iron atoms are circled in yellow. d) High magnification STEM-HAADF image and atomic resolution EDS elemental mapping showing the elemental distribution in a Fe/C_2N sample.

X-ray photoelectron spectroscopy (XPS) confirmed the Fe concentration to be around 1 wt% (Figure S4a, Supporting Information). Additionally, XPS was used to analyze the sample chemical structure. The high-resolution N 1s XPS spectrum was fitted with three bands at 406.5, 402.5, and 399.6 eV, which correspond to oxidized nitrogen (406.5 and 402.5 eV)[35,51] and pyrazine nitrogen (399.6 eV)[43] (Figure S4b, Supporting Information). The C1s XPS spectrum was resolved into four bands (Figure S4c, Supporting Information), associated to C=C (284.3 eV), C−N (285.1 eV), C=O (287.3 eV), and the C-heteroatom (288.9 eV).[26] The high resolution Fe 2p XPS spectrum (Figure S4d, Supporting Information) was fitted with 4 bands corresponding to two iron oxidation states. The main two bands were located at 724 eV ($2p_{1/2}$) and 710 eV ($2p_{3/2}$) and corresponded to a Fe^{2+} chemical state. The second doublet at 712.7 eV ($2p_{1/2}$) and 726.5 eV ($2p_{3/2}$) was assigned to satellite peaks.[35] From the linear combination fitting, the average valence state of the Fe atom is +1.767.

To further reveal the chemical structure of Fe/C_2N and particularly the valence state of iron, X-ray absorption near-edge structure (XANES) analyses were carried out using an Fe foil and Fe_2O_3 as references. As shown in **Figure 2**a, the edge structure of Fe/C_2N in the XANES spectra is much closer to that of Fe_2O_3 than to Fe, meaning that the valence state of Fe in Fe/C_2N is higher than that of the metallic state, consistently with XPS results. The XANES spectrum of Fe/C_2N also displayed a small peak at 7112.9 eV, which is similar to that in iron phthalocyanine.[34,45] This peak indicated the presence of a Fe−N bond in Fe/C_2N catalysts.[35] Fourier transform was applied to the extended X-ray absorption fine structure (FT-EXAFS) spectra shown in Figure 2b and further used to investigate the coordination structure of Fe/C_2N. For the Fe foil, the main peak at 2.2 Å stands for the Fe−Fe bond, while for the Fe_2O_3, the peaks at 1.5 and 2.6 Å are associated to Fe−O and Fe−Fe bonds, respectively.[36,46] The FT-EXAFS

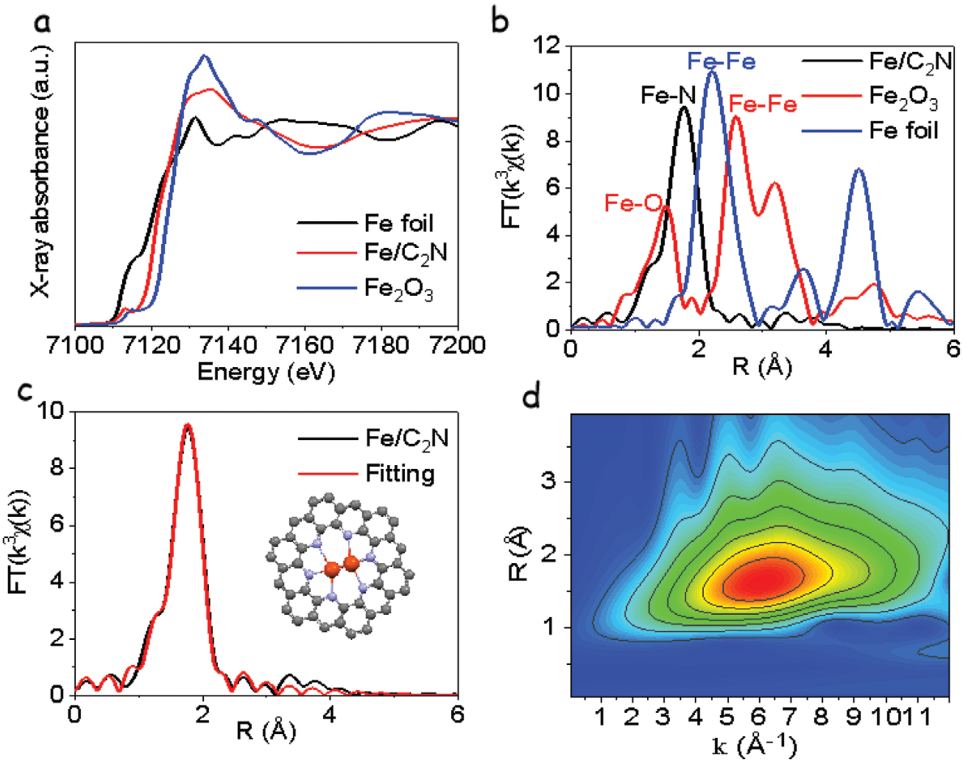

Figure 2. a) XANES spectra of a Fe/C_2N sample and the reference Fe foil and Fe_2O_3. b) k3-weighted FT-EXAFS spectra corresponding to the Fe K-edge. c) EXAFS fitting curves in R space for the Fe/C_2N sample. d) Wavelet transform plot for Fe/C_2N.

spectrum of Fe/C_2N displayed a peak at 1.76 Å, in between that of Fe—Fe and Fe—O bonds. This peak was attributed to a Fe—N bond, demonstrating the coordination of iron with nitrogen in Fe/C_2N. To obtain a higher detail of the Fe coordination within Fe/C_2N, the EXAFS spectra at the Fe K-edge was fitted (Figure 2c and Table S1: Supporting Information). Fitting results showed that the coordination number of Fe—N is 3, and the average coordination number of Fe—Fe is 1.5, which discarded the presence of iron and iron oxide nanoparticles, consistently with SEM-EDX, HRTEM, XRD, and XPS results. Notice that the coordination number of Fe—Fe bond in our EXAFS fitting results is 1.5, which is consistent with HAADF-AC-STEM results, further confirming the successful iron atomic dispersion.[37]

A wavelet transform (WT) analysis of the K3-weight EXAFS signal was carried out to further characterize the atom back scattering (Figure 2d and Figure S5: Supporting Information). The reference Fe foil exhibited a WT maximum at 8.0 $Å^{-1}$, associated to Fe–Fe. The reference Fe_2O_3 exhibited two WT maxima, at 8.0 and 4.0 $Å^{-1}$, corresponding to Fe—Fe and Fe—O, respectively. Instead, Fe/C_2N displayed a single WT maximum located at 5.9 $Å^{-1}$, which was assigned to Fe–N.

To investigate the performance of Fe/C_2N as sulfur host in LSB cathodes, Fe/C_2N composites were loaded with ≈70 wt% of elemental sulfur using the melt-impregnation method. In the following, the Fe/C_2N sample loaded with elemental sulfur will be named as S@Fe/C_2N. The XRD pattern obtained on the S@Fe/C_2N sample (Figure 1d) displayed the peak corresponding to the orthorhombic sulfur phase, confirming the presence of sulfur. TGA quantified the final percentage of sulfur in the S@Fe/C_2N composite to be 69 wt% (Figure S6a, Supporting Information). EDX analysis showed the sulfur to be uniformly distributed on the surface of Fe/C_2N (Figure S6b, Supporting Information). The Brunauer–Emmett–Teller (BET) specific surface area of Fe/C_2N was 223.4 $m^2\ g^{-1}$, and it decreased with the sulfur loading to the 13.1 $m^2\ g^{-1}$ measured for S@Fe/C_2N. In parallel, the overall pore volume decreased from 0.10 to 0.04 $cm^3\ g^{-1}$ after sulfur loading. These results further confirmed sulfur to be infiltrated in the material cavities and pores (Figure S7, Supporting Information).[23]

We evaluated the ability of Fe/C_2N to adsorb LiPS by immersing the same amount (20 mg) of Super P, C_2N and Fe/C_2N into a 10×10^{-3} M solution of Li_2S_4. After 24 h, the solutions containing C_2N and Fe/C_2N were completely transparent, while the blank solution and the solution containing Super P showed a dark orange color (**Figure 3**a). These results demonstrate the excellent ability of C_2N-based materials for LiPS adsorption. The high-resolution Fe 2p and N 1s XPS spectra obtained on the Fe/C_2N before and after Li_2S_4 adsorption are displayed in Figure 3b,c. After Li_2S_4 adsorption, the Fe 2p and N 1s peaks showed a significant shift to higher binding energies, which denoted a strong chemical interaction between Li_2S_4 and Fe/C_2N

To further investigate the strong interaction between LiPS and Fe/C_2N, density functional theory (DFT) calculations were conducted. For comparison, the interaction between LiPS and C_2N was also calculated. Based on the XPS and XAFS results,

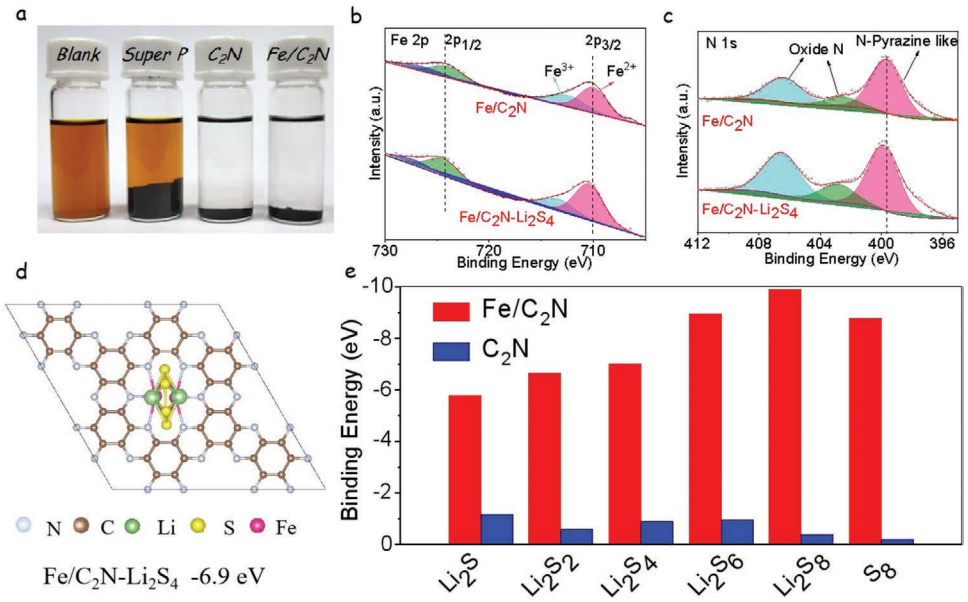

Figure 3. a) Adsorption test: Digital photograph of the Li_2S_4 solution before and after (24 h) the addition of Super P, C_2N and Fe/C_2N, as marked in each flask cap. b) High resolution XPS spectra of Fe 2p from Fe/C_2N before and after the Li_2S_4 adsorption test. c) High resolution XPS spectra of N 1s obtained on the Fe/C_2N sample before and after the Li_2S_4 adsorption test. d) Adsorption configurations for Li_2S_4 on Fe/C_2N. e) Binding energies between LiPS (Li_2S, Li_2S_2, Li_2S_4, Li_2S_6, Li_2S_8, and S_8) and C_2N or Fe/C_2N as calculated by DFT.

the Fe–Fe double atom on C_2N was used as model for the DFT calculations and C_2N as reference (Figure S8, Supporting Information). Figure 3d shows the optimized adsorption configuration with Li_2S_4. Figure S9 (Supporting Information) exhibits the optimized adsorption configuration with LiPS species (Li_2S, Li_2S_2, Li_2S_4, Li_2S_6, Li_2S_8, and S_8) on C_2N and Fe/C_2N. The corresponding binding energies are displayed in Figure 3e. DFT calculations showed the absolute binding energies for Fe/C_2N with LiPS species to be higher than those for C_2N, indicating that Fe/C_2N has a stronger ability to absorb soluble LiPS. These results are consistent with the absorption test of Li_2S_4, suggesting that Fe/C_2N could be effective to suppress the "shuttle effect" of LiPS.

To prove the electrocatalytic activity of Fe/C_2N for polysulfide conversion, CV tests of symmetric cells with identical working and counter electrodes were conducted in 0.5 M Li_2S_6. Electrodes were prepared using a slurry-casting process. Fe/C_2N-based electrodes displayed two cathodic and two anodic symmetric peaks at ±0.13 and ±0.08 V (**Figure 4**a), which are associated with the electrochemical oxidation and reduction of

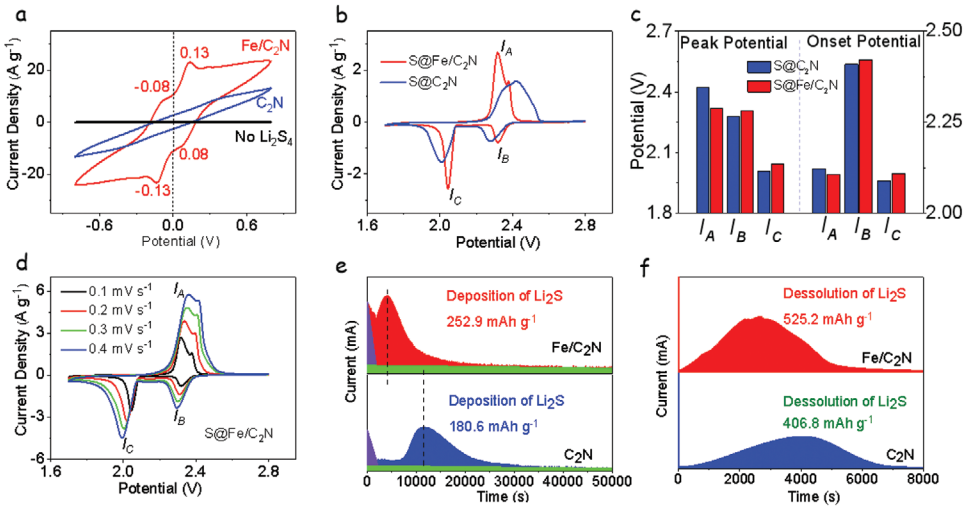

Figure 4. a) CV curves of symmetrical cells with 20 mV s^{-1} scan rate. b) CV profiles of Li–S cells with S@Fe/C_2N and S@C_2N cathodes with 0.1 mV s^{-1} scan rate. c) Peak potential and onset potential of asymmetrical Li–S cells based on the CV curves. d) CV profiles of the S@Fe/C_2N electrode with scan rates from 0.1 to 0.4 mV s^{-1}. e) Potentiostatic discharge profiles at 2.04 V on Fe/C_2N and C_2N electrodes with Li_2S_8 catholyte. f) Potentiostatic charge profiles at 2.32 V to evaluate the dissolution kinetics of Li_2S.

Li_2S_6.[38,39] More specifically, the cathodic peak at –0.13 V and the anodic peak at 0.13 V are related to the reaction

$$S_6^{2-} + 10e^- + 12Li^+ \leftrightarrow 6Li_2S \quad (1)$$

and the cathodic peak at 0.08 V and the anodic peak at –0.08 V to the reaction

$$4S_6^{2-} \leftrightarrow 8e^- + 3S_8 \quad (2)$$

On the other hand, redox peaks were barely observed in the CV profiles of symmetrical cells based on C_2N. C_2N-based cells were also characterized by much lower current densities than those based on Fe/C_2N.

With the Fe/C_2N-based electrode, redox peaks were clearly defined even when the scanning rate was increased from 10 to 100 mV s^{-1} (Figure S10a, Supporting Information). These results pointed out the important role played by the atomically dispersed Fe on the catalytic reaction of polysulfides. Besides, the excellent overlapping of the CV curves obtained from symmetric cells based on Fe/C_2N electrodes indicated excellent process reversibility and cell stability (Figure S10b, Supporting Information).

Electrochemical impedance spectroscopy (EIS) analysis (Figure S10c, Supporting Information) showed the charge transfer resistance of the Fe/C_2N-based electrode to be much lower than that of C_2N. Here it is important to take into account that the activation process is also related to the decreasing of the charge-transfer resistance after cycling. Therefore, our results provide strong evidence that the Fe/C_2N based electrodes have a better reaction response than that of the C_2N electrodes between polysulfides and Li_2S_2/Li_2S during charging and discharging process.

CV curves of Li–S coin cells based on S@Fe/C_2N and S@C_2N cathodes are shown in Figure 4b. These CV curves were found to almost overlap during the first cycles, indicating good reversibility of the sulfur redox reaction (Figure S11, Supporting Information). S@Fe/C_2N-based cells displayed a peak at 2.32 V (I_B) during the cathodic scan attributed to the transformation reactions

$$S_8 + 2e^- + 2Li^+ \rightarrow Li_2S_8 \quad (3)$$

$$3Li_2S_8 + 2e^- + 2Li^+ \rightarrow 4Li_2S_6 \quad (4)$$

$$2Li_2S_6 + 2e^- + 2Li^+ \rightarrow 3Li_2S_4 \quad (5)$$

The second reduction peak in the cathodic scan at 2.04 V (I_C) corresponds to the reactions[40,41]

$$Li_2S_4 + 2e^- + 2Li^+ \rightarrow 2Li_2S_2 \quad (6)$$

$$Li_2S_2 + 2e^- + 2Li^+ \rightarrow 2Li_2S \quad (7)$$

For the S@C_2N-based cells, cathodic peaks appeared broader and shifted to lower potentials, 2.3 V (I_B) and 2.0 V (I_C).

During the anodic scan, S@Fe/C_2N cells displayed two overlapping peaks at 2.35–2.40 V (I_A) that are attributed to the oxidation reaction from Li_2S_2/L_2S to S_8. Broader peaks, shifted around 50 mV to higher potentials (2.40–2.45 V) were obtained for the S@C_2N cell. Overall, S@Fe/C_2N cathodes displayed cathodic peaks at a more positive potential and anodic peaks at more negative potentials than S@C_2N, suggesting improved kinetics for the polysulfide transformation reaction (Figure 4c). The catalytic activity of Fe/C_2N electrode was quantified through the onset potential at a current density of 10 μA cm^{-2} beyond the baseline current (Figure S12, Supporting Information). As displayed in Figure 4c, S@Fe/C_2N cathodes were characterized by higher onset potentials for the reduction peaks and lower onset potentials for the oxidation peaks, further demonstrating the important catalytic role played by the atomically dispersed iron in S@Fe/C_2N cathodes.

CV measurements at various scanning rates, from 0.1 to 0.4 mV s^{-1}, were conducted to explore the reaction kinetics. As shown in Figure 4d and Figure S13a (Supporting Information), an increase of the scan rate did not modify the shape of the redox peaks, indicating good electrochemical stability. The linear relationship between the potential of the reduction and oxidation peak maxima and the square root of the scan rate pointed toward a diffusion-limited process (Figure S13b, Supporting Information). Thus, the Li^+ ion diffusion coefficients (D_{Li+}) were calculated through the Randles–Sevcik equation[42,44]

$$I_P = \left(2.69 \times 10^5\right) n^{1.5} S D_{Li^+}{}^{0.5} C_{Li^+} v^{0.5} \quad (8)$$

where I_P represents the peak current, n is the electron transferred number, S is the geometric area of the electrode, D_{Li+} represents the lithium ion diffusion coefficient, $C_{Li}{}^+$ is the concentration of lithium ions and v is the potential scanning rate. n, S, and $C_{Li}{}^+$ are constant in this equation, so D_{Li+} can be determined from the slope of I_P versus $v^{0.5}$. Slopes of the cathodic and anodic peaks were significantly higher for S@Fe/C_2N (Figure S13c–e, Supporting Information) than for S@C_2N electrodes, implying higher D_{Li+} values for the former (Figure S13f, Supporting Information). This result suggested a faster transport of lithium ions and a related more efficient conversion of polysulfides in S@Fe/C_2N than in S@C_2N electrodes.

To further evaluate the catalytic effect of the electrode materials on the reversible reaction between polysulfide and Li_2S, potentiostatic nucleation and dissolution experiments were carried out. As shown in Figure 4d, the deposition of Li_2S on Fe/C_2N electrodes was considerably faster and at a larger current density under 2.05 V than on C_2N. Based on Faraday's law, the Fe/C_2N electrode exhibited a precipitation capacity of 252.9 mAh g^{-1}, well above that of the C_2N electrode (180.8 mAh g^{-1}). Similarly, the potentiostatic Li_2S dissolution experiment (Figure 4e) showed the Fe/C_2N electrode to be characterized by a much higher current density and dissolution capacity (525.2 mAh g^{-1}) than C_2N (406.8 mAh g^{-1}). These results further proved that the atomically dispersed iron in C_2N enhanced the deposition and kinetic dissolution of Li_2S.

Overall, the dispersion of iron atoms not only provided strong polysulfide interaction sites through the enhancement of the C_2N polarity, but also acted as excellent active sites for the reversible transformation of Li_2S.

DFT calculations were conducted to reveal in detail the redox kinetics of the LiPS conversion. **Figure 5**a and Figure S14

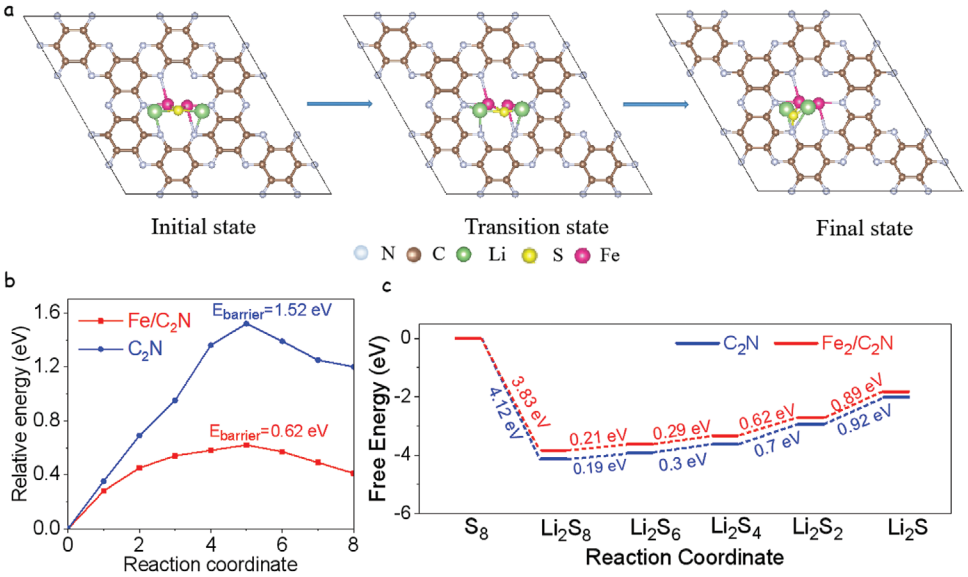

Figure 5. a) The optimized adsorption configuration of Li_2S decomposition on Fe/C_2N. b) Energy barrier profiles of Li_2S cluster decomposition on C_2N and Fe/C_2N along with different reaction coordinates. c) Energy profiles of the reduction of Fe/C_2N and C_2N substrate respectively.

(Supporting Information) exhibit the initial state, transition state and final state of Li_2S decomposition on Fe/C_2N and C_2N. The calculated energy barrier for Li_2S decomposition on Fe/C_2N and C_2N surface was 0.62 and 1.52 eV, respectively (Figure 5b). These results demonstrate that Fe/C_2N can greatly reduce the Li_2S decomposition energy barrier and enhance the redox reversibility between Li_2S and LiPSs. Next, the Gibbs free energies were calculated for the S reduction pathways of both $S@C_2N$ and $S@Fe/C_2N$ cathodes. The optimized configuration of the intermediates and their Gibbs free energy profiles are exhibited in Figure 5c. The largest increase of Gibbs free energy was obtained for the conversion from Li_2S_2 to Li_2S species, suggesting this step as the rate-limiting for the total discharge process.[22] The free energy increase was lower for Fe/C_2N (0.89 eV) than for C_2N (0.92 eV), which suggested that the reduction of S is more thermodynamically favorable on Fe/C_2N than on C_2N substrate.

In **Figure 6**a, the galvanostatic charge-discharge curves for $S@Fe/C_2N$ and $S@C_2N$ electrodes at a current rate of 0.1 C are displayed. The voltage jump of the blue charging curve at the initial charging period reflects the overpotentials of Li_2S activation. This demonstrates that the C_2N electrode displays a higher overpotential than the Fe/C_2N electrode, verifying the accelerated activation process of Li_2S in the presence of Fe/C_2N. The discharging curve is associated with the multistep sulfur reaction mechanism. Two clear discharge and one charge plateaus are observed in both cases. The first discharge plateau, at around 2.3 V, is attributed to the reduction of sulfur to soluble LiPS ($S_8 \rightarrow S_6^{2-} \rightarrow S_4^{2-}$). The second discharge plateau, at about 2.1 V, corresponds to the conversion of soluble LiPS into lithium sulfide ($S_4^{2-} \rightarrow Li_2S_2 \rightarrow Li_2S$).[50] Defining Q_1 and Q_2 as the capacity of the first discharge and the second discharge plateaus, respectively, the ratio between Q_2 and Q_1 (Q_2/Q_1) can be considered as a measure of the catalytic activity of the electrode material. The higher the capacity ratio value, the better the catalytic ability.[47,48] Figure 6b shows the capacity ratio for the $S@Fe/C_2N$ electrode to be quite large ($Q_2/Q_1 = 2.86$), well above the ratio measured for the $S@C_2N$ electrode ($Q_2/Q_1 = 2.35$). This result is consistent with the superior catalytic activity of the Fe-loaded electrode toward the polysulfides redox reaction.

As shown in Figure 6b, the polarization potential, i.e., the difference between the oxidation potential and the second reduction potential, of the $S@Fe/C_2N$ electrode (ΔE = 142.3 mV) was significantly lower than that of the $S@C_2N$ electrode (ΔE = 180.9 mV). The lower overpotential for the phase conversion between soluble LiPS and insoluble Li_2S_2/Li_2S during the charge (Figure S15a, Supporting Information) and discharge (Figure S15b, Supporting Information) processes, further confirmed the improved redox kinetics of $S@Fe/C_2N$.

Figure 6c and Figure S15c (Supporting Information) exhibit the galvanostatic charge-discharge voltage profiles at various current densities ranging from 0.1 C to 5 C. The two discharge plateaus and the charge plateau were clearly observed even at the highest charge/discharge rates. Figure 6d shows the specific capacities at different discharge rates of the two electrode types tested. $S@Fe/C_2N$ cathodes were characterized with average discharge capacities of 1480, 1250, 1085, 955, 856.4, 774, and 683 mAh g^{-1} at current rates from 0.1 C to 5 C, well above the capacities obtained for $S@C_2N$ cathodes (Figure 6d). Besides, when switching back the current rate from 5 C to 0.2 C, fairly similar average capacities were recovered, 1172 mAh g^{-1} for the $S@Fe/C_2N$ electrode, which pointed toward an excellent stability.

The energy efficiency of the energy storage device was calculated using the following formula: $E = \int UIdt$. As shown in Figure 6e, the $S@Fe/C_2N$ electrode was characterized by higher energy efficiency, up to 93% at 0.1 C, than $S@C_2N$, which is consistent with the lower polarization potential of the former, in turn associated with the exceptional catalytic properties of Fe/C_2N.

The cycling performance of $S@Fe/C_2N$ and $S@C_2N$ electrodes at 1 C are shown in Figure 6f. $S@Fe/C_2N$ electrodes displayed not only twofold higher capacities than $S@C_2N$,

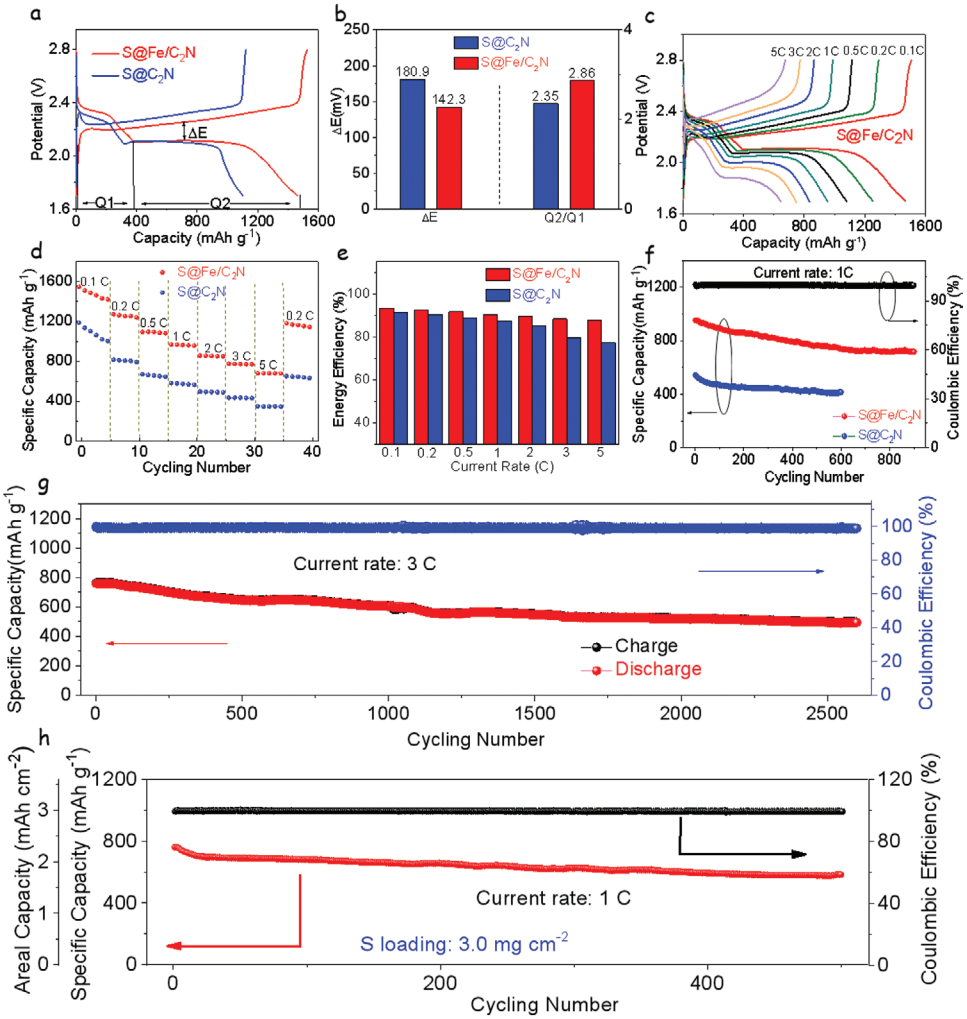

Figure 6. Electrochemical performance of Fe/C_2N and C_2N-based electrodes. a) Galvanostatic charge-discharge profiles of S@Fe/C_2N and S@C_2N electrodes with a 0.1 C current rate. b) Values of ΔE and Q_2/Q_1 resulted from the charge/discharge curves. c) Galvanostatic charge-discharge profiles of S@Fe/C_2N at various rates. d) Rate capabilities at current rates from 0.1 C to 5 C. e) Energy efficiency at various current rates. f) Capacity retention of S@Fe/C_2N and S@C_2N electrodes at 1 C. g) Capacity retention of S@Fe/C_2N electrode at 3 C. h) Capacity retention at 1 C with 3.0 mg cm^{-2} sulfur loading.

but also improved stability. S@Fe/C_2N electrodes maintained a discharge capacity of 716.5 mAh g^{-1} after 900 cycles, with a coulombic efficiency of 99.7%. This value corresponds to a capacity retention of 75.14%, i.e., an average capacity reduction rate of 0.0276% per cycle. Figure 6g displays the cycling performance of the S@Fe/C_2N electrode at 3 C current rate. At this high current rate, the initial discharge capacity was 764.1 mAh g^{-1}. After 2600 cycles, the capacity was still 496.5 mAh g^{-1}, which corresponds to a 0.013% average capacity attenuation per cycle.

Figure S16 (Supporting Information) displays results from EIS analysis before the first discharge and after 200 cycles at 1 C. Comparing the S@C_2N with the S@Fe/C_2N electrode, the latter showed a much lower R_{ct}, indicating improved electrode kinetics.

To explore the potential practical application of Fe/C_2N-based cathodes, electrodes with higher sulfur loading were produced and tested. Galvanostatic charging and discharging profiles at various current rates from a S@Fe/C_2N electrode with 3.0 mg cm^{-2} sulfur loading are shown in Figure S17a (Supporting Information). One charging plateau and two discharging plateaus were clearly observed even at current rates up to 3 C. The average specific capacities were 972 mAh g^{-1} at 0.1 C and 610 mAh g^{-1} at 3 C, corresponding to areal capacities of 2.8 and 1.8 mAh cm^{-2}, respectively. Figure S17b (Supporting Information) shows the rate performances of the S@Fe/C_2N electrode with a high sulfur load, which displayed average discharge capacities of 1189.5, 966, 839.5, 734.7, 680.6, 601.3, and 605 mAh g^{-1} at current rates from 0.1 C to 3 C. Besides, the long-term cycling test of this electrode displayed the initial capacity of 760 mAh g^{-1} to decrease at a rate of 0.046% per cycle to 584.6 mAh g^{-1} after 500 cycles, which corresponds to a 76.92% capacity retention (Figure 6h). During this process, a coulombic efficiency above 99.3% was maintained. These results suggest our materials show excellent LSBs performance (Table S2, Supporting Information).

To further analyze the advantages of Fe/C_2N for efficient LSBs performance,[52] an EDS mapping of the Li-anode after cycling was conducted. On the EDS maps, only a very small amount of sulfur was observed (Figure S18, Supporting Information), which means that the Fe/C_2N as cathode in the LSBs can inhibit the "shuttle effect" of the polysulfides efficiently. On the other hand, SEM characterization (Figure S19, Supporting Information) of the cathode after cycling was also performed. At the full-discharged state of 1.7 V, the cells were disassembled to investigate the morphology of Fe/C_2N after cycling. The corresponding SEM image displayed nanoparticles that were uniformly distributed on the surface of Fe/C_2N rather than aggregating into large bulk agglomerates. Combined with the Li_2S nucleation measurement through potentiostatic discharge profiles, the results further demonstrated that Fe/C_2N catalyst regulate the deposition behavior of Li_2S. To evaluate the stability of the Fe/C_2N structure during cycles, we conducted XRD measurements (Figure S20, Supporting Information) of the cathode after charging. Diffraction peaks corresponding to Fe nanoparticles or aggregates were not observed, meaning that the atomically dispersed iron atoms, which act as active sites, are kept stable and isolated during cycling.

Overall, the above results demonstrate that Fe/C_2N-based cathodes show an excellent electrochemical performance associated to the following properties: 1) The abundant presence of pyrazine nitrogen and pores in the C_2N structure, which can immobilize LiPS and thus minimize the shuttle effect; 2) The high electrical conductivity of Fe/C_2N which maximizes the sulfur utilization; and 3) The presence of atomically dispersed iron, which is coordinated to nitrogen and work as efficient active sites to promote the polysulfide conversion reaction kinetics.

3. Conclusions

In summary, a novel catalyst based on atomically dispersed iron in a 2D organic material (Fe/C_2N) has been shown as an efficient sulfur host material for LSBs. A combination of XPS, XANES, EXAFS, atomic resolution HAADF-AC-STEM, and DFT calculations confirmed that the synthesized Fe/C_2N presents atomically dispersed iron. Iron atoms, which are in some cases found to group in pairs, are coordinated to nitrogen in the C_2N pores. These atomically dispersed Fe atoms not only improve the material polarity to immobilize the soluble polysulfides, but also act as catalytic active sites to promote the reaction kinetics between sulfur, polysulfide, and Li_2S. As a result, S@Fe/C_2N-based cathodes exhibit excellent electrochemical performance, showing a high capacity and a remarkable rate performance at different current densities, while keeping outstanding cycling stability. This work demonstrates that atomically dispersed metal atoms within the unique C_2N structure can help to achieve excellent electrochemical performance. The present strategy can be utilized to design active materials not only for LSBs, but also for other energy conversion and storage systems.

4. Experimental Section

Materials: Ethylenediamine (99%), 1,3-dioxolane (DOL, 99.5%), lithium nitrate (99.98%), lithium sulfide (99.9%), and chloroanilic acid (98%) were purchased from Alfa Aesar. Sulfuric acid (95–98%), *N*-methyl-pyrrolidone (NMP, 99.99%), diethyl ether (99.9%), iron (III) nitrate nonahydrate (>98%), and tetraethylene glycol dimethyl ether (99%) were purchased from Sigma-Aldrich. Lithium bis(trifluoromethanesulfonyl) imide (LiTFSI) (99%) was purchased from Acros Organics and dimethoxymethane (DME, 99%) is from Honeywell. All chemicals were used without further purification.

Synthesis of Hexaaminobenzene (HAB): First,[32] chloroanilic acid was placed into a 15 mL glass vial which was put in a 0 °C ice bath, under vigorous stirring. Next, 5.64 mL ethylenediamine and a few drops of concentrated sulfuric acid were added. Then the ice bath was removed and the obtained solution was warmed up to room temperature. Afterward, the solution was transferred to a 15 mL Teflon autoclave, the autoclave was kept at 80 °C for 72 h to complete the amination reactions. The solution was cooled to room temperature. The obtained mixture was vacuum filtrated using a polytetrafluoroethylene (PTFE) membrane (0.47 µm), rinsed with diethyl ether and degassed ethanol three times, and freeze-dried overnight. The identity of the final product was confirmed by ^{1}H NMR. ^{1}H NMR (400 MHz, H_2O-d_2, δ): 3.39 (s, 2H, NH2) (Figure S21, Supporting Information).

Synthesis of C_2N: In a typical reaction experiment,[33] an equal mol ratio of hexaaminobenzene and chloroanilic acid, and degassed NMP were put into a three-necked round bottom flask under argon gas placed in an ice bath. Under vigorous stirring, a few drops of concentrated sulfuric acid were added. Then the ice bath was removed and the mixture was warmed up to room temperature. The resulting solution was heated to 175 °C for 12 h. After cooling to room temperature, the mixture was vacuum filtrated, and washed with ethanol and water for three times and freeze-dried for 24 h. Finally, the obtained black solid was annealed at 450 °C for 3 h under argon gas with a ramp rate of 5 °C min^{-1}.

Synthesis of Fe/C_2N: C_2N (200 mg) and iron(III) nitrate nonahydrate (404 mg) were added to 15 mL ethanol. The resulting solution was stirred for 48 h at room temperature, and then vacuum filtrated and dried at 60 °C in an oven. The obtained precursor was annealed at 700 °C for 3 h. After that, the black solid was placed into 10 mL 3 M HCl solution and stirred for 2 days to remove iron nanoparticles. The material was centrifuged, washed with water and ethanol for several times, and finally vacuum dried at 120 °C for 12 h.

Preparation of S@C_2N and S@Fe/C_2N Composites: Following a typical melt-diffusion procedure, Fe/C_2N (or C_2N) was mixed with sublimated sulfur in a mass ration of 1:3 through uniform milling, then transferred to a clean vial, placed in a Teflon autoclave, sealed under argon gas and heated for 12 h at 155 °C. To remove the redundant sulfur outside of the Fe/C_2N, the powder was immersed in a 10 mL CS_2 and ethanol solution (1:4, volume ratio) for 10 min twice.

Li_2S_4 Adsorption Tests: Sulfur and Li_2S with a molar ratio of 3:1 were mixed with appropriate amounts of DME and DOL (volume ratio of 1:1) under vigorous stirring overnight, until a homogeneous dark brown solution was formed. To test the adsorption ability for polysulfide, 20 mg active materials (Fe/C_2N, C_2N, and Super P) were covered by a 3.0 mL 10×10^{-3} M Li_2S_4 solution in a glass vial, kept shaking and ageing overnight.

Electrochemical Measurements: To prepare the cathodes, active materials (S@C_2N, S@Fe/C_2N), Super P and PVDF binders were mixed with a mass ratio of 8:1:1 dispersing in N-methyl-2-pyrrolidone (NMP, 99.99%, Sigma-Aldrich). The obtained homogeneous slurry was cast on an aluminum foil current collector and then vacuum dried at 60 °C overnight. The sulfur was loaded in small plates (with a diameter of 12 mm) and was stamped in a coated aluminum film with about 1 mg cm^{-2}. For the high sulfur loading, a coating of 3.0 mg cm^{-2} was used. The coin cells were assembled in an argon-filled glove box for the electrochemical tests. The anode used was a Li foil and Celgard 2400 membranes were used as separators. 1.0 M lithium bis(trifluoromethanesulfony) imide (LiTFSI) and 0.2 M $LiNO_3$ dissolved in the mixed solvent of DOL and DME (1:1 v/v) were used as the electrolyte. Each coin cell contained about 20 µL of the electrolyte. To allow the electrolyte to penetrate the electrode sufficiently, all coin cells were aged for several hours before testing.

Galvanostatic charge/discharge (GCD) measurements were conducted between 1.7 and 2.8 V (vs Li^+/Li) in a Neware BTS4008 battery cycler. A battery tester BCS-810 from BioLogic was used to perform the cyclic voltammetry (CV) tests with different scan rates, ranging from 0.1 to 0.4 mV s^{-1}. Electrochemical impedance spectroscopy (EIS) tests were conducted in the frequency range from100 kHz to 0.01 Hz.

Symmetric Cell Assembly and Tests: Electrode for the symmetric cell were prepared using the same method as that for the lithium-sulfur battery. The working and counter electrodes utilized two pieces of the same electrode (with an average loading of ≈0.5 mg cm^{-2}). Each coin cell contained 40 µL of electrolyte (0.5 M Li_2S_6 and 1 M LiTFSI in DOL/DME (v/v = 1/1)). CV tests were carried out at a scan rate of 10 mV s^{-1} and EIS measurements were performed in a frequency range from 100 kHz to 0.01 Hz.

Li_2S_2 Nucleation and Dissolution Tests: Standard 2032 coin cells were used to analyze the nucleation and dissolution of the Li_2S. Equal amounts of Fe/C_2N and C_2N catalysts were dispersed uniformly in ethanol. Then, the catalysts were loaded on carbon paper to work as cathodes. Li foil worked as anode. The catholyte consisted of 20 µL of 0.25 M Li_2S_8 and 1.0 M LiTFSI in tetraethylene glycol dimethyl ether solution. In the case of the anolyte, it consisted of 20 µL of 1.0 M LiTFSI solution without Li_2S_8 in the same solvent as the catholyte. To transform the polysulfide Li_2S_x ($x = 6, 8$) to Li_2S_4 the following procedure was used. The cells were kept at 2.05 V until the current dropped to 0.01 mA. Fresh coin cells were assembled to perform the dissolution of Li_2S, which were discharged at 0.10 mA to 1.80 V first, following galvanostatically discharge at 0.01 mA to 1.80 V for reducing S species into solid Li_2S, completely. Subsequently, the cells were potentiostatically charged at 2.40 V for transforming the Li_2S into polysulfide until the charge current was lower than 0.01 mA.[49]

Supporting Information

Supporting Information is available from the Wiley Online Library or from the author.

Acknowledgements

Z.L., D.Y., and P.T. contributed equally to this work. ICN2 is supported by the Severo Ochoa program from Spanish MINECO (Grant No. SEV-2017-0706) and is funded by the CERCA Programme/Generalitat de Catalunya. Part of the present work has been performed in the framework of Universitat Autònoma de Barcelona Materials Science PhD program. J.D. has received funding from the European Union's Horizon 2020 research and innovation programme under the Marie Sklodowka-Curie grant agreement No 665919 (P-SPHERE) co-funded by Severo Ochoa Programme. Z.L. acknowledges funding from MINECO SO-FPT PhD grant (SEV-2013-0295-17-1). This project has received funding from the European Union's Horizon 2020 research and innovation programme under grant agreement No 823717-ESTEEM3. The present work is supported by the European Regional Development Funds and by the Spanish MINECO through the projects SEHTOP, ENE2016-77798-C4-3-R, and ENE2017-85087-C3. D.Y., X.W., and C.Z. thank the China Scholarship Council for the scholarship support. P.T. acknowledges Humboldt Research Fellowship for Postdoctoral Researchers sponsored by the Alexander von Humboldt Foundation. J.L. obtained International Postdoctoral Exchange Fellowship Program (Talent-Introduction program) in 2019 and is grateful for the project (2019M663468) funded by the China Postdoctoral Science Foundation. Authors acknowledge funding from Generalitat de Catalunya 2017SGR327 and 2017SGR1246. J.L. is a Serra Húnter Fellow and is grateful to MICINN/FEDER RTI2018-093996-B-C31, GC 2017 SGR 128 and to ICREA Academia program. The authors thank Jessica Padilla, Dr. Albert Llorente Mola, and Dr. Tariq Jawhari support in ICN2, IREC and UB, respectively for the help in additional analyses performed in the samples.

Conflict of Interest

The authors declare no conflict of interest.

Keywords

atomically dispersed iron, electrocatalytic polysulfide conversion, lithium–sulfur batteries, organic layered materials

Received: November 6, 2020
Revised: November 24, 2020
Published online: December 18, 2020

[1] H.-J. Peng, J.-Q. Huang, X.-B. Cheng, Q. Zhang, *Adv. Energy Mater.* **2017**, *7*, 1700160.
[2] A. Manthiram, S. H. Chung, C. Zu, *Adv. Mater.* **2015**, *27*, 1980.
[3] P. G. Bruce, S. A. Freunberger, L. J. Hardwick, J. M. Tarascon, *Nat. Mater.* **2011**, *11*, 19.
[4] L. Lin, F. Pei, J. Peng, A. Fu, J. Cui, X. Fang, N. Zheng, *Nano Energy* **2018**, *54*, 50.
[5] J. Song, M. J. Choo, H. Noh, J. K. Park, H. T. Kim, *ChemSusChem* **2014**, *7*, 3341.
[6] Q. Pang, X. Liang, C. Y. Kwok, L. F. Nazar, *Nat. Energy* **2016**, *1*, 16132.
[7] M. Hagen, D. Hanselmann, K. Ahlbrecht, R. Maça, D. Gerber, J. Tübke, *Adv. Energy Mater.* **2015**, *5*, 1401986.
[8] B. Zhang, X. Qin, G. R. Li, X. P. Gao, *Energy Environ. Sci.* **2010**, *3*, 1531.
[9] J.-Z. Wang, L. Lu, M. Choucair, J. A. Stride, X. Xu, H.-K. Liu, *J. Power Sources* **2011**, *196*, 7030.
[10] G. Li, W. Lei, D. Luo, Y.-P. Deng, D. Wang, Z. Chen, *Adv. Energy Mater.* **2018**, *8*, 1702381.
[11] Y. S. Su, A. Manthiram, *Chem. Commun.* **2012**, *48*, 8817.
[12] P. Wei, M. Q. Fan, H. C. Chen, X. R. Yang, H. M. Wu, J. Chen, T. Li, L. W. Zeng, C. M. Li, Q. J. Ju, D. Chen, G. L. Tian, C. J. Lv, *Renewable Energy* **2016**, *86*, 148.
[13] H. Liao, H. Wang, H. Ding, X. Meng, H. Xu, B. Wang, X. Ai, C. Wang, *J. Mater. Chem. A* **2016**, *4*, 7416.
[14] T. Sun, J. Xie, W. Guo, D. S. Li, Q. Zhang, *Adv. Energy Mater.* **2020**, *10*, 1904199.
[15] Y. Yang, G. Zheng, Y. Cui, *Chem. Soc. Rev.* **2013**, *42*, 3018.
[16] X. Zhou, J. Tang, J. Yang, J. Xie, B. Huang, *J. Mater. Chem. A* **2013**, *1*, 5037.
[17] X. G. Sun, X. Wang, R. T. Mayes, S. Dai, *ChemSusChem* **2012**, *5*, 2079.
[18] F. Sun, J. Wang, H. Chen, W. Li, W. Qiao, D. Long, L. Ling, *ACS Appl. Mater. Interfaces* **2013**, *5*, 5630.
[19] Y. Cao, C. Liu, M. Wang, H. Yang, S. Liu, H. Wang, Z. Yang, F. Pan, Z. Jiang, J. Sun, *Energy Storage Mater.* **2020**, *29*, 207.
[20] X. Chen, Y. Xu, F. H. Du, Y. Wang, *Small Methods* **2019**, *3*, 1900338.
[21] J. Wang, L. Jia, J. Zhong, Q. Xiao, C. Wang, K. Zang, H. Liu, H. Zheng, J. Luo, J. Yang, H. Fan, W. Duan, Y. Wu, H. Lin, Y. Zhang, *Energy Storage Mater.* **2019**, *18*, 246.
[22] Z. Du, X. Chen, W. Hu, C. Chuang, S. Xie, A. Hu, W. Yan, X. Kong, X. Wu, H. Ji, L. J. Wan, *J. Am. Chem. Soc.* **2019**, *141*, 3977.
[23] J. Xie, B. Q. Li, H. J. Peng, Y. W. Song, M. Zhao, X. Chen, Q. Zhang, J. Q. Huang, *Adv. Mater.* **2019**, *31*, 1903813.
[24] L. Zhang, D. Liu, Z. Muhammad, F. Wan, W. Xie, Y. Wang, L. Song, Z. Niu, J. Chen, *Adv. Mater.* **2019**, *31*, 1903955.
[25] Y. Li, J. Wu, B. Zhang, W. Wang, G. Zhang, Z. W. Seh, N. Zhang, J. Sun, L. Huang, J. Jiang, J. Zhou, Y. Sun, *Energy Storage Mater.* **2020**, *30*, 250.
[26] J. Mahmood, F. Li, S. M. Jung, M. S. Okyay, I. Ahmad, S. J. Kim, N. Park, H. Y. Jeong, J. B. Baek, *Nat. Nanotechnol.* **2017**, *12*, 441.

[27] J. Mahmood, S.-M. Jung, S.-J. Kim, J. Park, J.-W. Yoo, J.-B. Baek, *Chem. Mater.* **2015**, *27*, 4860.
[28] J. Mahmood, F. Li, C. Kim, H.-J. Choi, O. Gwon, S.-M. Jung, J.-M. Seo, S.-J. Cho, Y.-W. Ju, H. Y. Jeong, G. Kim, J.-B. Baek, *Nano Energy* **2018**, *44*, 304.
[29] J. Xu, J. Mahmood, Y. Dou, S. Dou, F. Li, L. Dai, J. B. Baek, *Adv. Mater.* **2017**, *29*, 1702007.
[30] J. Wu, L.-W. Wang, *J. Mater. Chem. A* **2018**, *6*, 2984.
[31] H. Lin, R. Jin, A. Wang, S. Zhu, H. Li, *Ceram. Int.* **2019**, *45*, 17996.
[32] S. S. Shinde, C. H. Lee, J.-Y. Jung, N. K. Wagh, S.-H. Kim, D.-H. Kim, C. Lin, S. U. Lee, J.-H. Lee, *Energy Environ. Sci.* **2019**, *12*, 727.
[33] S. S. Shinde, C. H. Lee, J. Y. Yu, D. H. Kim, S. U. Lee, J. H. Lee, *ACS Nano* **2018**, *12*, 596.
[34] N. Ramaswamy, U. Tylus, Q. Jia, S. Mukerjee, *J. Am. Chem. Soc.* **2013**, *135*, 15443.
[35] F. Xiao, G.-L. Xu, C.-J. Sun, M. Xu, W. Wen, Q. Wang, M. Gu, S. Zhu, Y. Li, Z. Wei, X. Pan, J. Wang, K. Amine, M. Shao, *Nano Energy* **2019**, *61*, 60.
[36] A. Zitolo, V. Goellner, V. Armel, M. T. Sougrati, T. Mineva, L. Stievano, E. Fonda, F. Jaouen, *Nat. Mater.* **2015**, *14*, 937.
[37] W. Ye, S. Chen, Y. Lin, L. Yang, S. Chen, X. Zheng, Z. Qi, C. Wang, R. Long, M. Chen, J. Zhu, P. Gao, L. Song, J. Jiang, Y. Xiong, *Chem* **2019**, *5*, 2865.
[38] H. Lin, L. Yang, X. Jiang, G. Li, T. Zhang, Q. Yao, G. W. Zheng, J. Y. Lee, *Energy Environ. Sci.* **2017**, *10*, 1476.
[39] H. Lin, S. Zhang, T. Zhang, H. Ye, Q. Yao, G. W. Zheng, J. Y. Lee, *Adv. Energy Mater.* **2019**, *9*, 1902096.
[40] S. S. Zhang, *J. Power Sources* **2013**, *231*, 153.
[41] Y. Li, J. Fan, J. Zhang, J. Yang, R. Yuan, J. Chang, M. Zheng, Q. Dong, *ACS Nano* **2017**, *11*, 11417.
[42] X. Zhu, W. Zhao, Y. Song, Q. Li, F. Ding, J. Sun, L. Zhang, Z. Liu, *Adv. Energy Mater.* **2018**, *8*, 1800201.
[43] J. Mahmood, E. K. Lee, M. Jung, D. Shin, I.-Y. Jeon, S. M. Jung, H-.J. Choi, J.-M. Seo, S.-Y. Bae, S. D. Sohn, N. Park, J. H. Oh, H.-J. Shin, J. B. Baek, *Nat. Commun.* **2015**, *6*, 6486.
[44] G. Zhou, H. Tian, Y. Jin, X. Tao, B. Liu, R. Zhang, Z. W. Seh, D. Zhuo, Y. Liu, J. Sun, J. Zhao, C. Zu, D. S. Wu, Q. Zhang, Y. Cui, *Proc. Natl. Acad. Sci. USA* **2017**, *114*, 840.
[45] J. F. Kimer, W. Dow, W. R. Scheidt, *Inorg. Chem.* **1976**, *15*, 1685.
[46] Y. Chen, S. W. Ji, Y. Dong, J. Chen, W. Li, Z. Shen, R. Zheng, L. Zhuang, Z. Wang, Y. D. Li, *Angew. Chem., Int. Ed.* **2017**, *129*, 7041.
[47] D. Su, M. Cortie, H. Fan, G. Wang, *Adv. Mater.* **2017**, *29*, 1700587.
[48] C.-Y. Fan, Y.-P. Zheng, X.-H. Zhang, Y.-H. Shi, S.-Y. Liu, H.-C. Wang, X.-L. Wu, H.-Z. Sun, J.-P. Zhang, *Adv. Energy Mater.* **2018**, *8*, 1703638.
[49] C. Zhang, J. J. Biendicho, T. Zhang, R. Du, J. Li, X. Yang, J. Arbiol, Y. Zhou, J. R. Morante, A. Cabot, *Adv. Funct. Mater.* **2019**, *29*, 1903842.
[50] H. Yuan, H.-J. Peng, B.-Q. Li, J. Xie, L. Kong, M. Zhao, X. Chen, J.-Q. Huang, Q. Zhang, *Adv. Energy Mater.* **2019**, *9*, 1802768.
[51] W. Cheng, L.u. Weng, Y. Li, A. Lau, C. K. Chan, C. Chan, *Aerosol Sci. Technol.* **2013**, *47*, 1118.
[52] J.-Y. Wei, X.-Q. Zhang, L.-P. Hou, P. Shi, B.-Q. Li, Y. Xiao, C. Yan, H. Yuan, J.-Q. Huang, *Adv. Mater.* **2020**, *32*, 2003012.

ADVANCED ENERGY MATERIALS

Supporting Information

for *Adv. Energy Mater.,* DOI: 10.1002/aenm.202003507

Atomically dispersed Fe in a C_2N Based Catalyst as a Sulfur Host for Efficient Lithium–Sulfur Batteries

Zhifu Liang, Dawei Yang, Pengyi Tang, Chaoqi Zhang, Jordi Jacas Biendicho, Yi Zhang, Jordi Llorca, Xiang Wang, Junshan Li, Marc Heggen, Jeremy David, Rafal E. Dunin-Borkowski, Yingtang Zhou, Joan Ramon Morante, Andreu Cabot,* and Jordi Arbiol**

Supporting Information

Atomically dispersed Fe in a C_2N based Catalyst as a Sulfur Host for Efficient Lithium-Sulfur Batteries

Zhifu Liang[+], Dawei Yang[+], Pengyi Tang[+], Chaoqi Zhang, Jordi Jacas Biendicho, Yi Zhang, Jordi Llorca, Xiang Wang, Junshan Li, Marc Heggen, Jeremy David, Rafal E. Dunin-Borkowski, Yingtang Zhou, Joan Ramon Morante, Andreu Cabot*, Jordi Arbiol**

Z.F Liang, Dr. J. David, Prof. J. Arbiol

Catalan Institute of Nanoscience and Nanotechnology (ICN2), CSIC and BIST

Campus UAB, Bellaterra, 08193 Barcelona, Catalonia, Spain

Email: arbiol@icrea.cat

Z.F Liang, D. W. Yang, C. Q. Zhang, X. Wang, Dr. J. Jacas Biendicho, Prof. J. R. Morante, Prof. A. Cabot

Catalonia Institute for Energy Research - IREC

Sant Adrià de Besòs, Barcelona, 08930, Catalonia, Spain

Email: acabot@irec.cat

Dr. P. Y Tang, Dr. M Heggen, Prof. R E. Dunin-Borkowski

Ernst Ruska-Centre for Microscopy and Spectroscopy with Electrons and Peter Grünberg Institute Forschungszentrum Jülich GmbH 52425 Jülich, Germany

Prof. Y. T. Zhou

Key Laboratory of Health Risk Factors for Seafood and Environment of Zhejiang Province

Institute of Innovation & Application

Zhejiang Ocean University, Zhoushan, Zhejiang Province, 316022, China

Email: zhouyingtang@zjou.edu.cn

Prof. J. Llorca
Institute of Energy Technologies, Department of Chemical Engineering and Barcelona Research Center in Multiscale Science and Engineering
Universitat Politècnica de Catalunya, EEBE, 08019 Barcelona, Spain

Dr. Yi Zhang

School of Energy Sciences and Engineering, Nanjing Tech University, Nanjing 211816, Jiangsu Province, China

Prof. J. Arbiol, Prof. A. Cabot

ICREA

Pg. Lluís Companys 23, 08010 Barcelona, Catalonia, Spain

Dr.Junshan Li

Institute of Fundamental and Frontier Sciences, University of Electronic Science and Technology of China, 610054 Chengdu, P. R. China

D. W. Yang, C. Q. Zhang, X. Wang, Prof. J. R. Morante
Department of Electronic and Biomedical Engineering
Universitat de Barcelona, 08028 Barcelona, Catalonia, Spain

[+] These authors contribute equally to this work

* Corresponding authors

Materials characterization: Crystal structures were characterized using powder XRD in a Bruker AXS D8 Advance X-ray diffractometer. (Cu-Kα radiation, λ = 1.5106 Å, 40 kV and 40 mA; Bruker, Germany). TGA was performed under air or nitrogen gas at a heating rate of 10 °C/min using a Thermogravimetric Analyzer Q200. SEM images were obtained in a ZEISS Auriga Field emission scanning electron microscopy (FE-SEM) operating at 20 kV. HRTEM studies were conducted in a FEI Tecnai F20 microscope at an operating voltage of 200 kV. HAADF-STEM images and elemental mapping were obtained in a spherical aberration-corrected transmission electron microscope FEI Titan 80-300 at 300 kV and FEI Titan G2 80-200 ChemiSTEM with four EDX detectors and operated at 200 kV. X-ray photoelectron spectroscopy (XPS) data was obtained by using 150 W and a Phoibos 150 MCD-9 detector. The XANES and EXAFS were performed at the Beijing Synchrotron Radiation Facility (BSRF). The obtained XAFS data were analyzed according the standard procedures using ATHENA program.[S0] The nitrogen adsorption-desorption isotherms were recorded in a Tristar II 3020 Micromeritics system at 77 K. The specific surface area and the pore size distribution were calculated by Brunauer–Emmett–Teller (BET) and Barrett-Joyner-Halenda (BJH) methods.

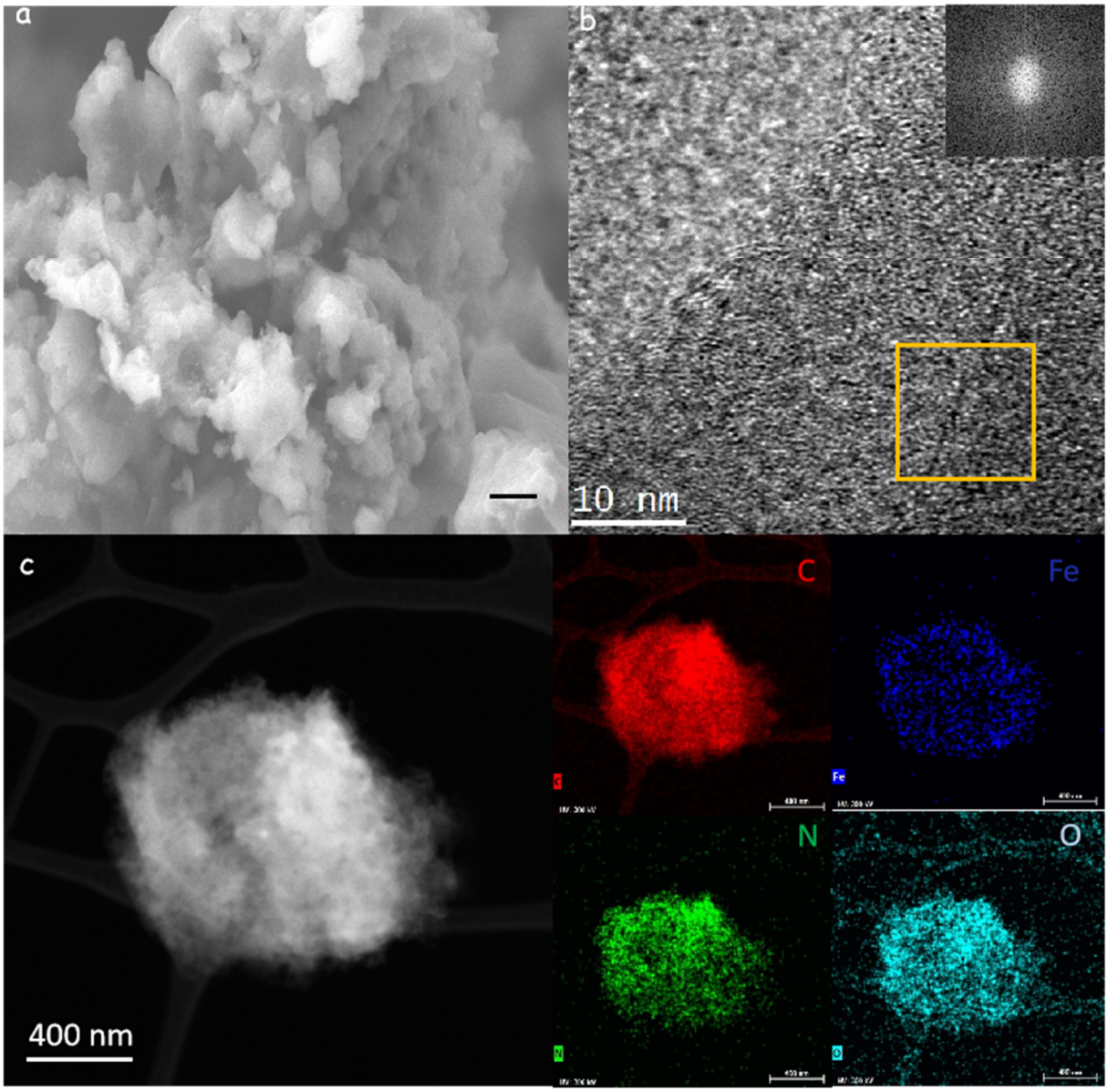

Figure S1. (a) SEM image of a Fe/C_2N catalyst (scale bar = 0.2 μm); (b) HRTEM image of a Fe/C_2N catalyst. (c) STEM-HAADF image and EDS elemental mapping (scale bar = 400 nm) showing the elemental distribution in a Fe/C_2N sample.

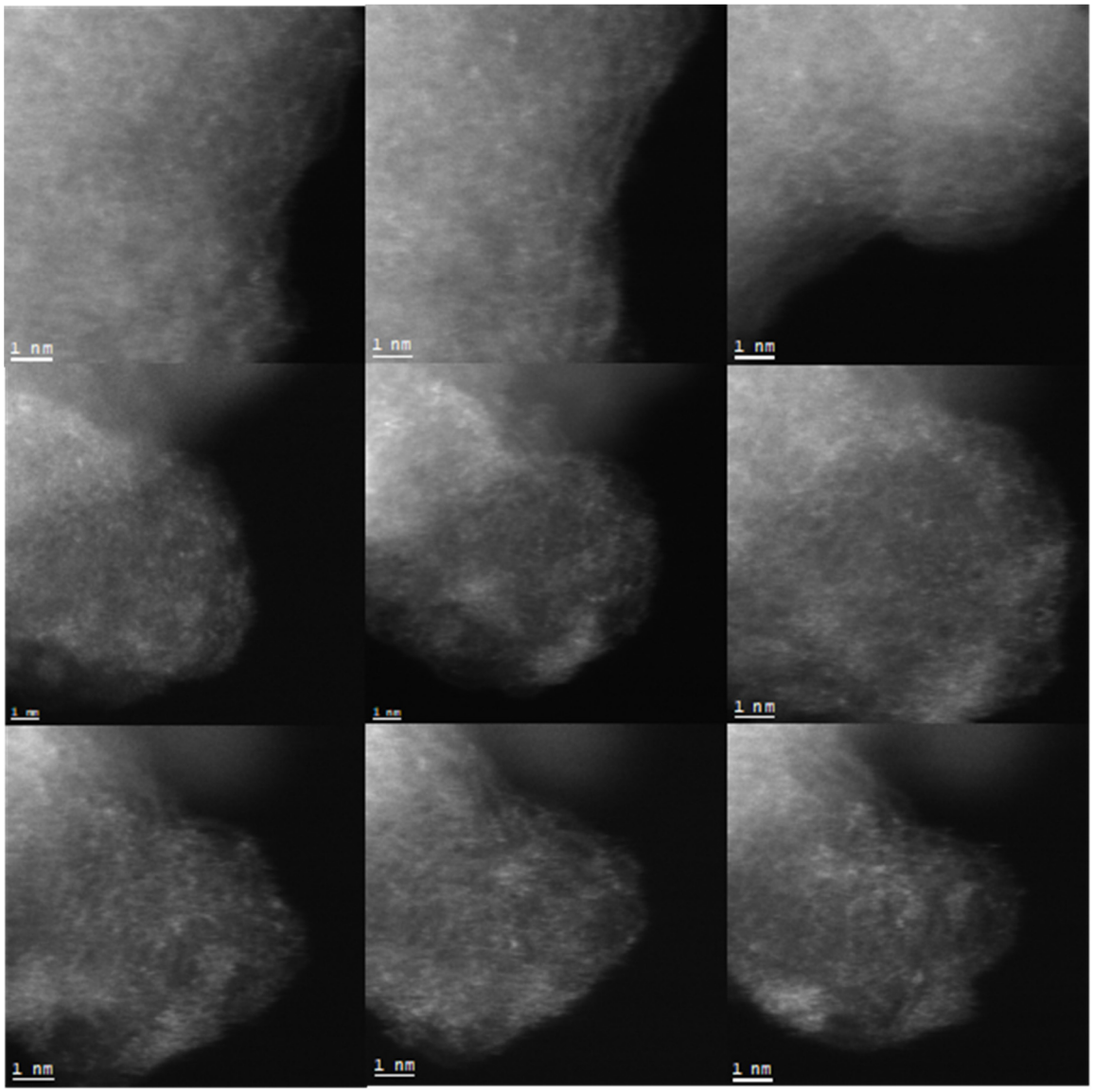

Figure S2. High magnification HAADF-STEM images of a Fe/C_2N catalyst.

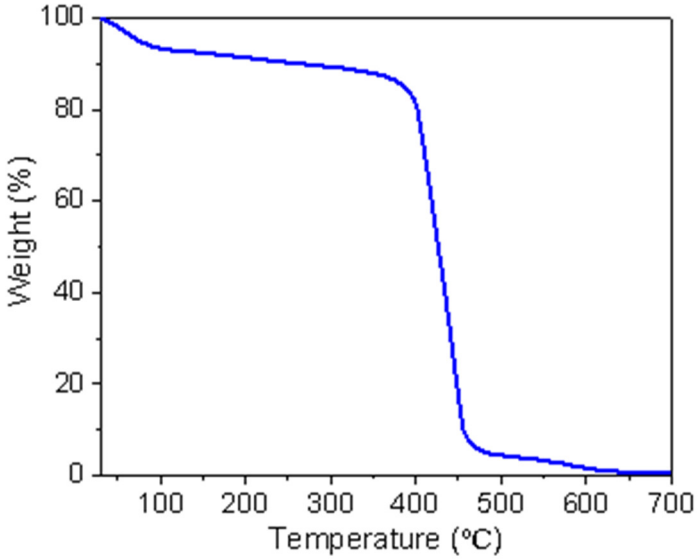

Figure S3. TGA profile of Fe/C_2N under air

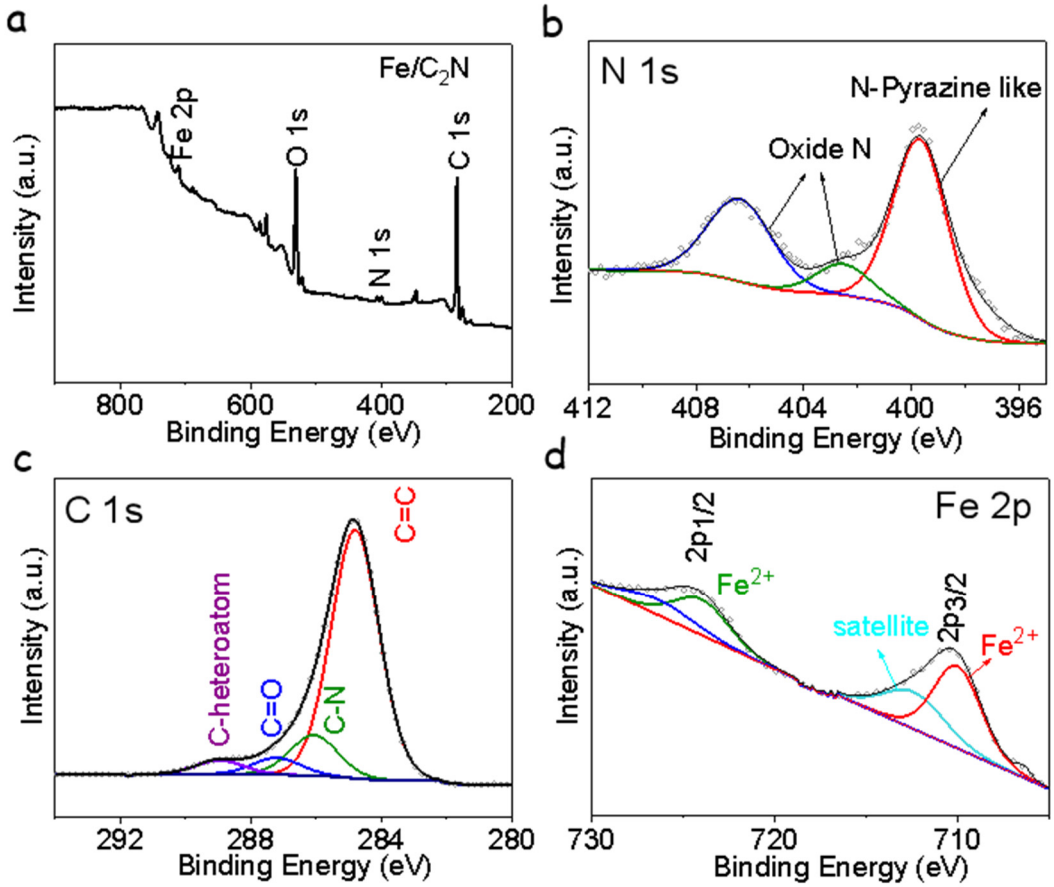

Figure S4. (a) XPS survey spectrum of Fe/C_2N. (b)-(d) High resolution XPS spectra obtained from Fe/C_2N: (b) N 1s; (c) C 1s ; (d) Fe 2p.

Table S1. EXAFS fitting parameters at the Fe K-edge for various samples（S_0^2=0.76）

	Shell	CN	R(Å)	σ2	ΔE0	R factor
Fe foil	Fe-Fe	8	2.46±0.01	0.0050	5.1±1.0	0.0055
	Fe-Fe1	6	2.84±0.01			
Fe/C_2N	Fe-N	3.0±0.1	1.97±0.02	0.0031	5.4±1.5	0.0016
	Fe-Fe	1.5±0.1	2.11±0.01	0.0029		

[a]*N*: coordination numbers; [b]*R*: bond distance; [c]σ^2: Debye-Waller factors; [d] ΔE_0: the inner potential correction. *R* factor: goodness of fit. S_0^2 was set to 0.76, according to the experimental EXAFS fit of Fe foil reference by fixing CN as the known crystallographic value; δ: percentage.

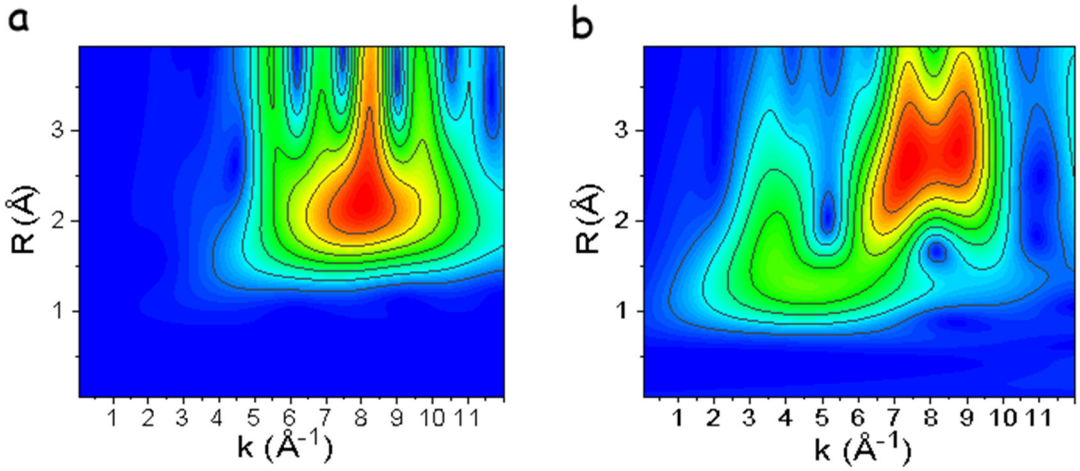

Figure S5. Wavelet tansforms for the k^3-weight Fe K-edge EXAFS information of reference samples: (a) Fe foil; (b) Fe_2O_3.

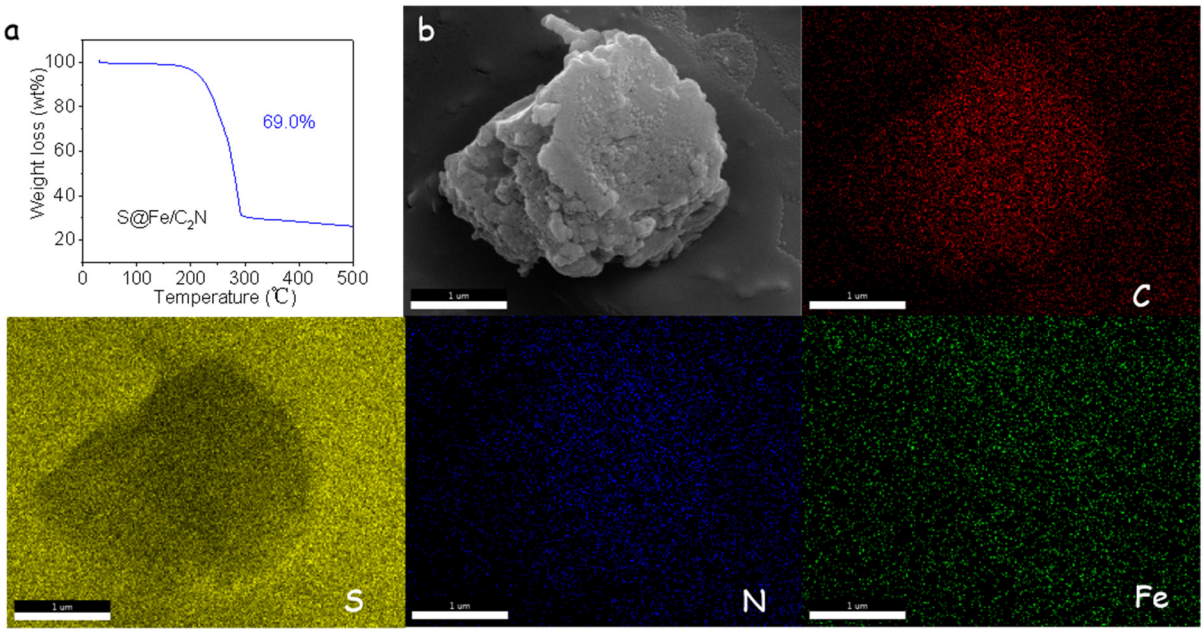

Figure S6. a) TGA profile from S@Fe/C_2N under nitrogen. (b) SEM EDX mapping of S@Fe/C_2N (scale bar = 1 μm).

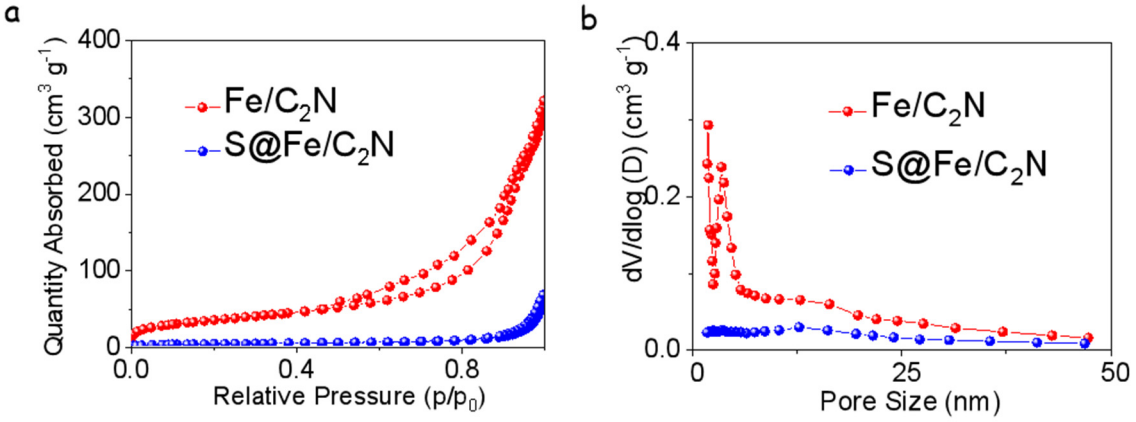

Figure S7. (a) N_2 adsorption-desorption isotherms of Fe/C_2N and S@Fe/C_2N. (b) Pore size distribution of Fe/C_2N and S@Fe/C_2N.

DFT Calculation

The spin-polarized DFT computations were implemented using the Perdew-Burke-Ernzerhof (PBE) functional, as performed in the VASP package.[S1] The project augmented wave (PAW) approach was used with a kinetic cutoff energy of 450 eV. According to previous literature,[S2] the molecule $C_{36}N_{12}H_{12}$ with one hole was used to represent the periodic C_2N system. Meanwhile, the model of Fe/C_2N(002) was constructed according the parameters of XRD and TEM as shown in **Figure S8a, 8b.** To avoid the neighboring image interactions, a 2×2×1 supercell of Fe/C_2N was created and a vacuum spacing of 15 Å was inserted along the normal direction. The first Brillouin zone was sampled with 3×3×1 and 5×5×1 Γ-centered k-points grids for geometric optimization and electronic structure calculations. All atoms were relaxed to their equilibrium positions when the total energy change was finally converged to 10^{-5} eV/atom; and the force on each atom was converged to 0.04 eV/Å. The adsorption energy (E_{ads}) is calculated through the following Equations based on the energy difference of the system before and after LIPS adsorption.[22]

$$E_{\text{ads}}(\text{C}_2\text{N}) = E_{total} - E_{Li_2S_x} - E_{\text{C}_2\text{N-surface}}$$

$$E_{\text{ads}}(\text{Fe}/\text{C}_2\text{N}) = E_{total} - E_{Li_2S_x} - E_{\text{Fe/C}_2\text{N-surface}}$$

Where the E_{Li2Sx}, $E_{surface}$, and E_{total} represent the total energy of the adsorbate, the surface, and the complex of surface and adsorbate, respectively. According to this formula, the more negative E_{ads} the better thermodynamic stability. The nudged elastic band (NEB) method was used to calculate the decomposition energy barriers of Li_2S.[S4] Finally, the Gibbs Free Energy was calculated basing the method in the reference 5. [S5]

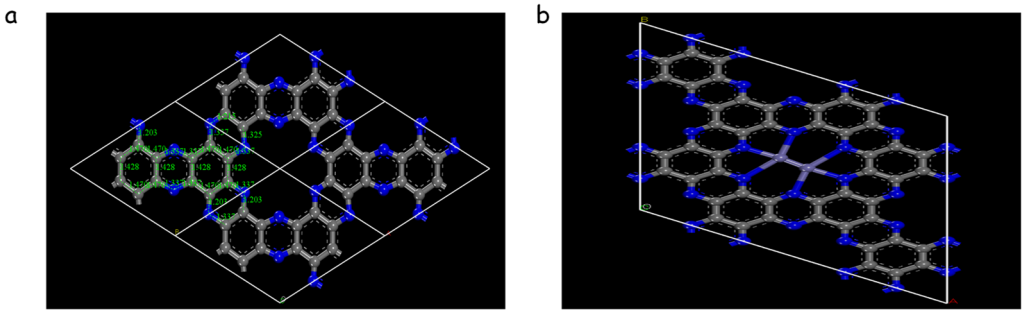

Figure S8. (a) Optimized C_2N monolayer, (b) Optimized Fe/C_2N monolayer. (grey = carbon; blue = nitrogen)

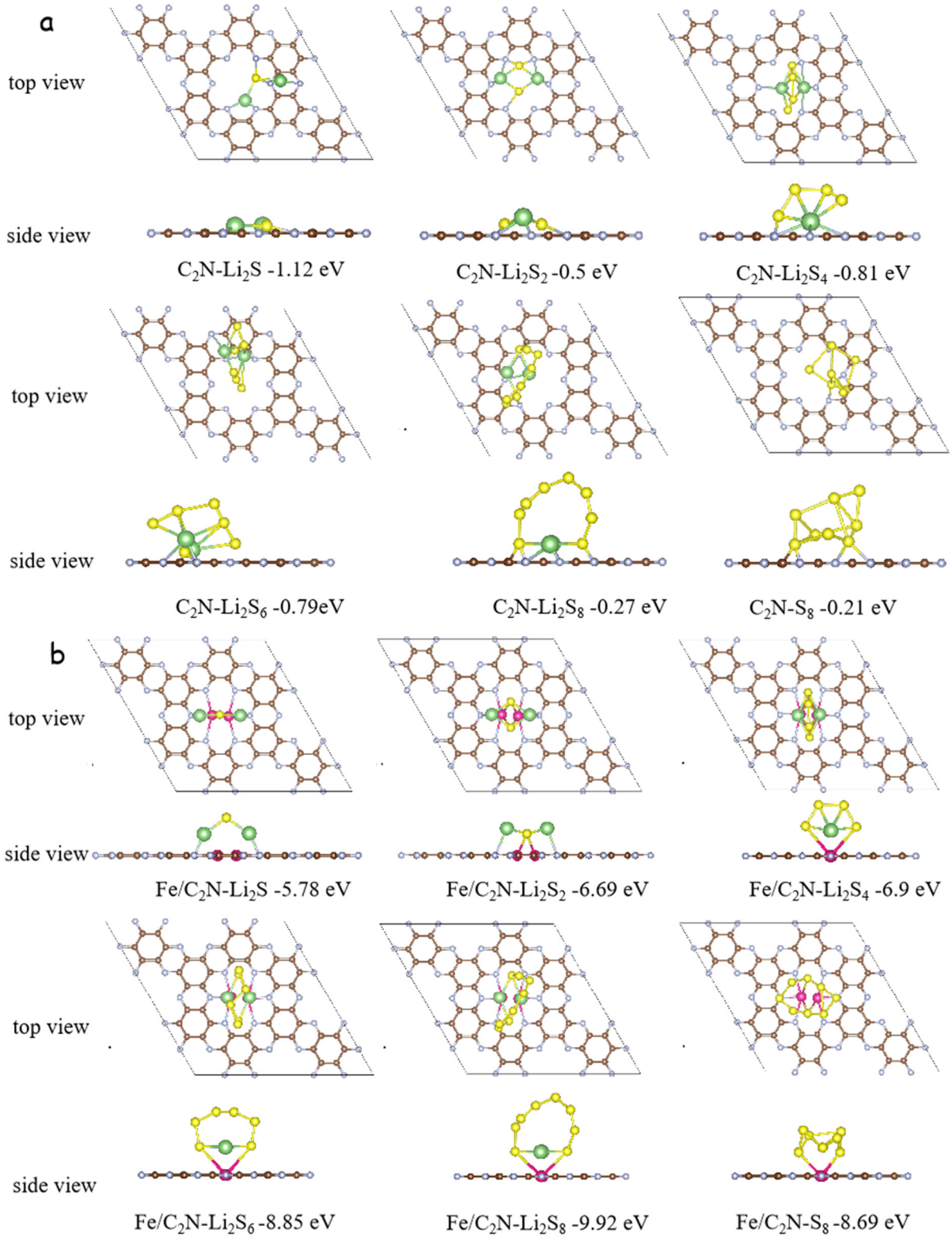

Figure S9. Schematic diagram of DFT calculation results for C_2N and Fe/C_2N with LiPS (Li_2S, Li_2S_2, Li_2S_4, Li_2S_6, Li_2S_8 and S_8): (a) C_2N. (b) Fe/C_2N. (light blue=nitrogen, brown=carbon, green=lithium, yellow=sulfur, pink=iron)

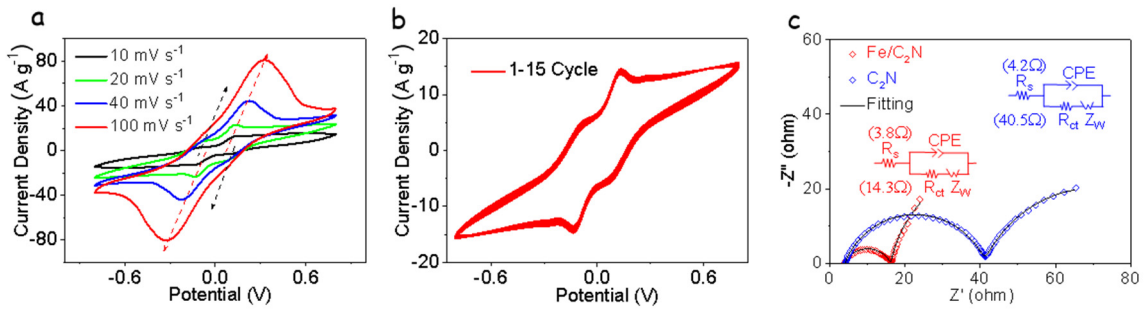

Figure S10. (a) CV profiles of S@C_2N electrode in symmetric cells at scan rate from 10 mV/s to 100 mV/s. (b) CV curves of symmetric cells from 1 to 15 cycles. (c) EIS spectrum of symmetric cells based on Fe/C_2N and C_2N sulfur host materials.

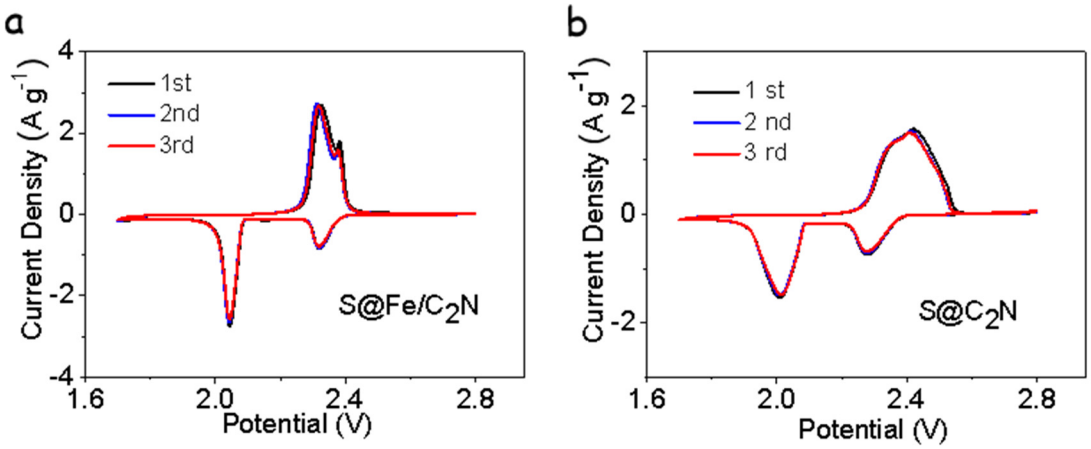

Figure S11. CV profiles of (a) S@Fe/C_2N, (b) S@C_2N with a scan rate of 0.1 mV s^{-1} in the potential range between 1.7 V and 2.8 V (vs Li/Li^+), each graph showing three cycles.

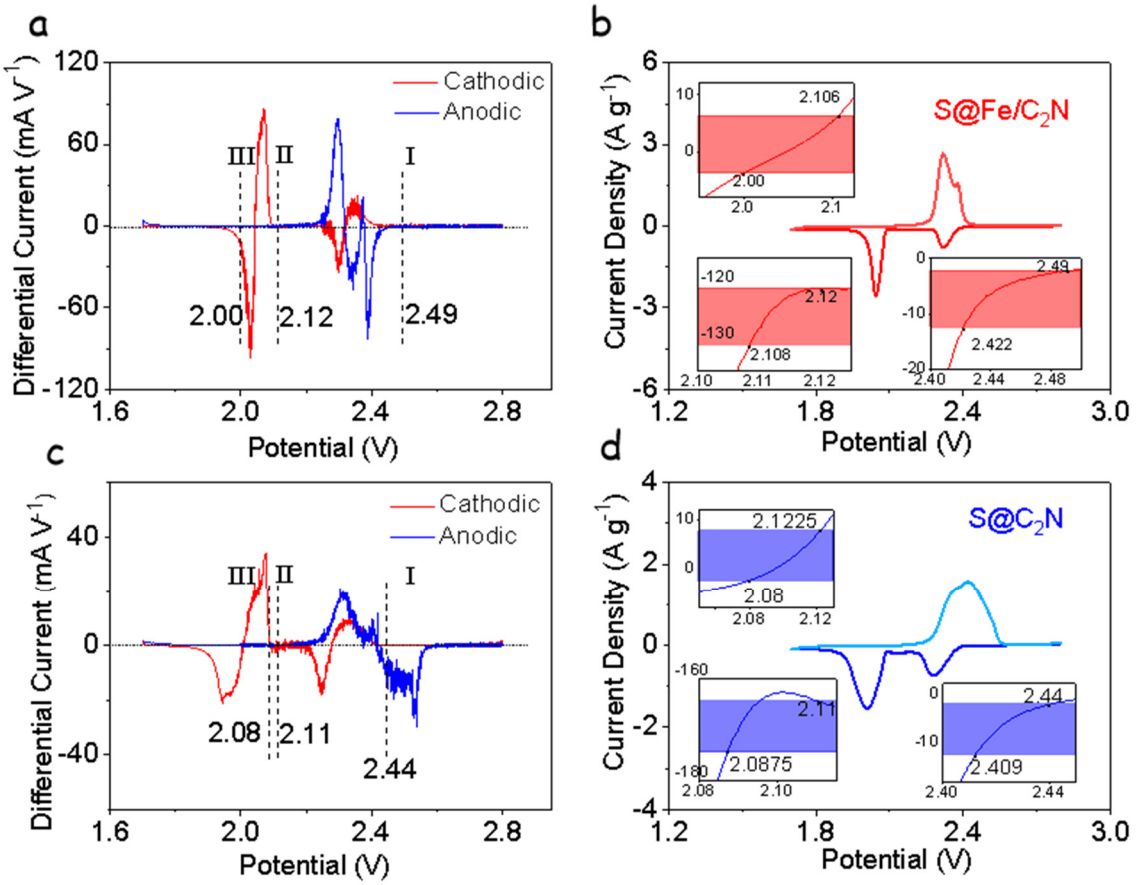

Figure S12. Onset potential for lithium-sulfur redox reaction. (a) Differential CV profiles of S@Fe/C_2N. (b) CV curves and corresponding onset potential of redox peak I, II and III of S@Fe/C_2N. (c) Differential CV profiles of S@C_2N. (b) CV curves and corresponding onset potential of redox peak I, II and III of S@C_2N.

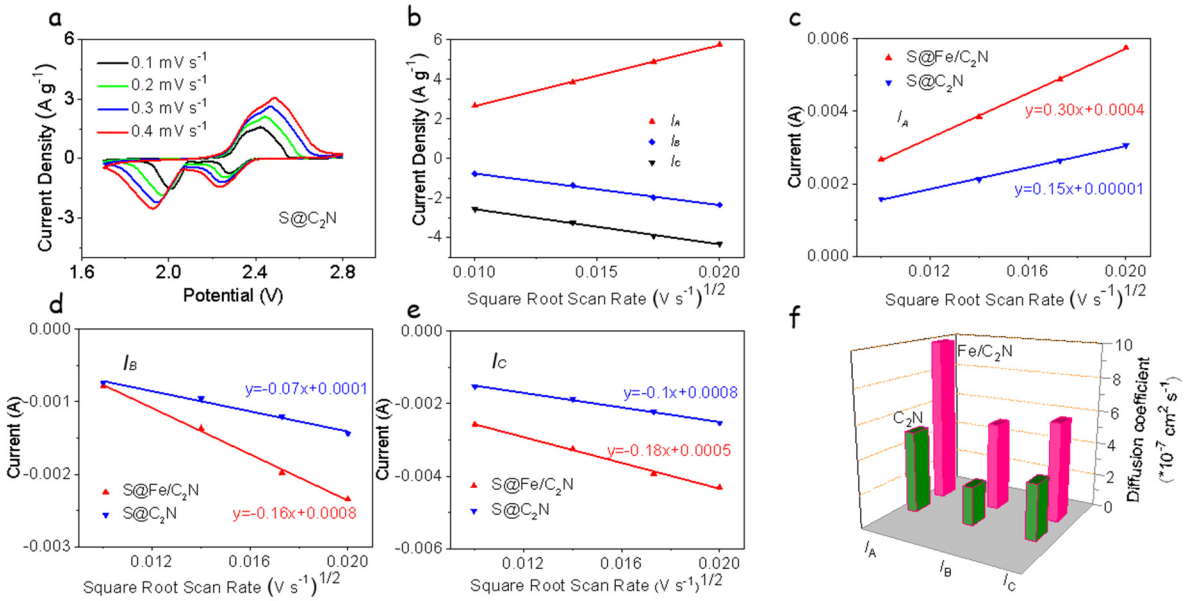

Figure S13. (a) CV profiles of S@C2N electrode at scan rate from 0.1 mV/s to 0.4 mV/s. (b) Plot of CV of S@Fe/C2N electrode peak current of I_A, I_B, I_C *vs* the square root of the scan rate. (c) Anodic oxidation reaction (peak I_A : $Li_2S_2/Li_2S \leftrightarrow S_8$) *vs* the square root of the scan rate. (d) First cathodic reduction process (peak I_B: $S_8 \leftrightarrow Li_2S_x$). (e) Second cathodic reduction reaction (peak I_C: $Li_2S_x \leftrightarrow Li_2S_2/Li_2S$). (f) Diffusion coefficient of S@Fe/C2N and S@C2N electrodes calculated from I_A, I_B, I_C respectively.

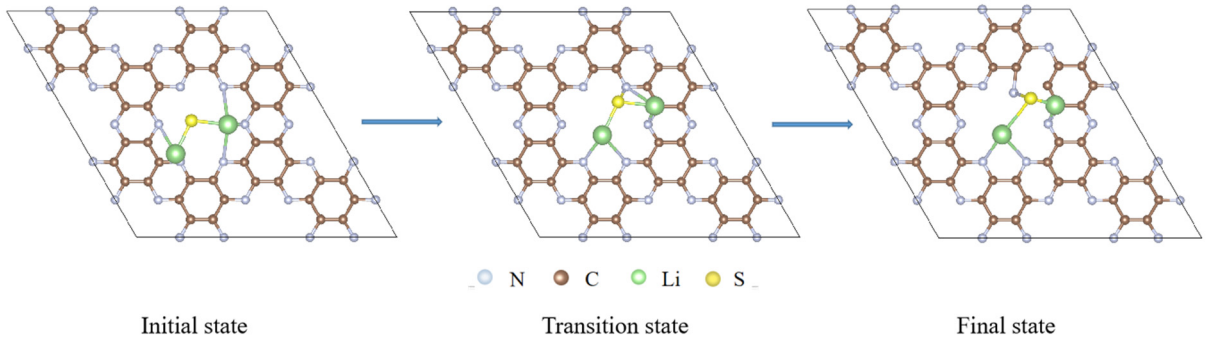

Figure S14. Schematic diagram of states of Li_2S decomposition on C_2N.

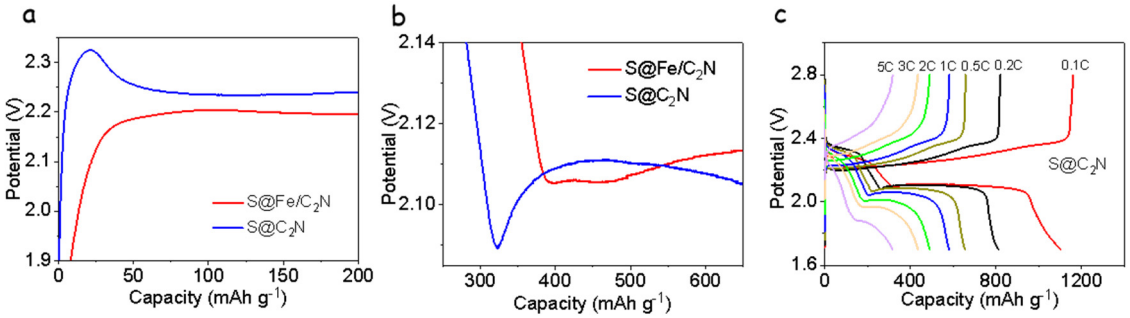

Figure S15. (a) Charge curves of S@Fe/C_2N and S@C_2N electrodes exhibiting the overpotentials for the transformation from Li_2Sx to Li_2S_2/Li_2S. (b) Discharge curves of S@Fe/C_2N and S@C_2N electrodes exhibiting the overpotentials for the transformation from Li_2S_2/Li_2S to Li_2S_x. (c) Charge/discharge curves of S@C_2N electrode at various current densities from 0.1 C to 5 C.

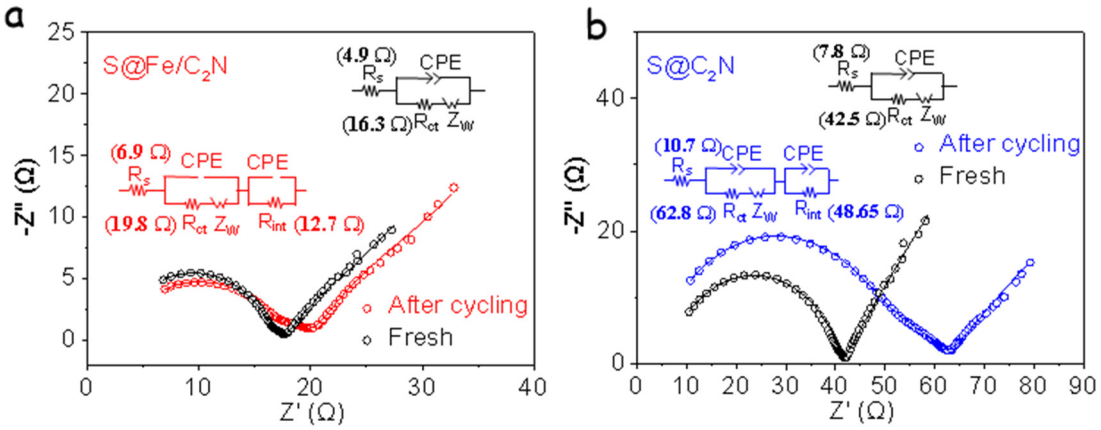

Figure S16. (a) EIS spectra obtained on coin cells fabricated with the S@Fe/C_2N cathode, for the fresh cell and after cycling at 1 C for 100 cycles respectively. (b) EIS spectra obtained on the coin cells fabricated with the S@C_2N cathode corresponding fresh cell and after cycling at 1 C for 100 cycles.

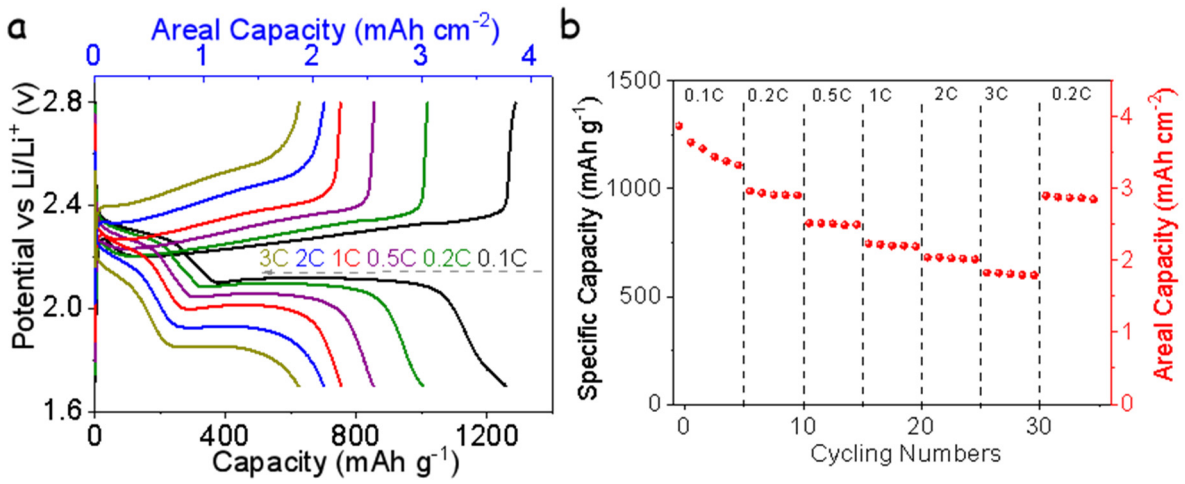

Figure S17. (a) Charge/discharge profiles. (b) Rate capability of S@Fe/C_2N electrode with sulfur loading of 3 mg cm^{-2} at different current densities.

Table S2. A summary of metal atom dispersed catalysts for LSBs

Reported materials	Coordination Structure	Initial capacity ($mAh\ g^{-1}$)	High rate capacity ($mAh\ g^{-1}$)	C rated/ cycle numbers	Capacity decay rate per cycle	Ref.
Fe/C_2N	Fe2N6	1540/0.1 C	678.7/5C	3 C/2600	0.013%	This work
Porous Fe-N2/CN	FeN2	1451/0.1 C	607/5 C	2 C/2000	0.011%	S5
Fe-N-doped carbon nanofiber	FeN4	1142/0.2 C	847/2 C	0.5 C/500	0.053%	S6
Fe-N-C/S-MCF	FeN4	1244/0.1 C	504/5 C	3 C/500	0.067%	S7
FeSA-CN	FeN4	1123/0.2 C	605/4 C	4 C/500	0.06%	S8
Fe-PNC	FeN4	1138/ 0.1 C	600/1 C	0.5 C/300	0.02%	S9
M-Co N-doped carbon	CoN4	1618/0.1 C	529/5 C	2C/1000	0.028%	S10
SC-Co	CoN4	1130/0.2 C	837/3 C	0.5 C/800	0.086%	23
Co-N/G	CoN4	1210/0.2 C	618/4 C	1 C/500	0.053%	22
H-Like Co@N-C	CoN4	1250/0.1 C	485/5C	2 C/850	0.02%	S11
CoSA-NC	CoN4	1574/0.05C	624/5 C	1 C/1000	0.03%	S12

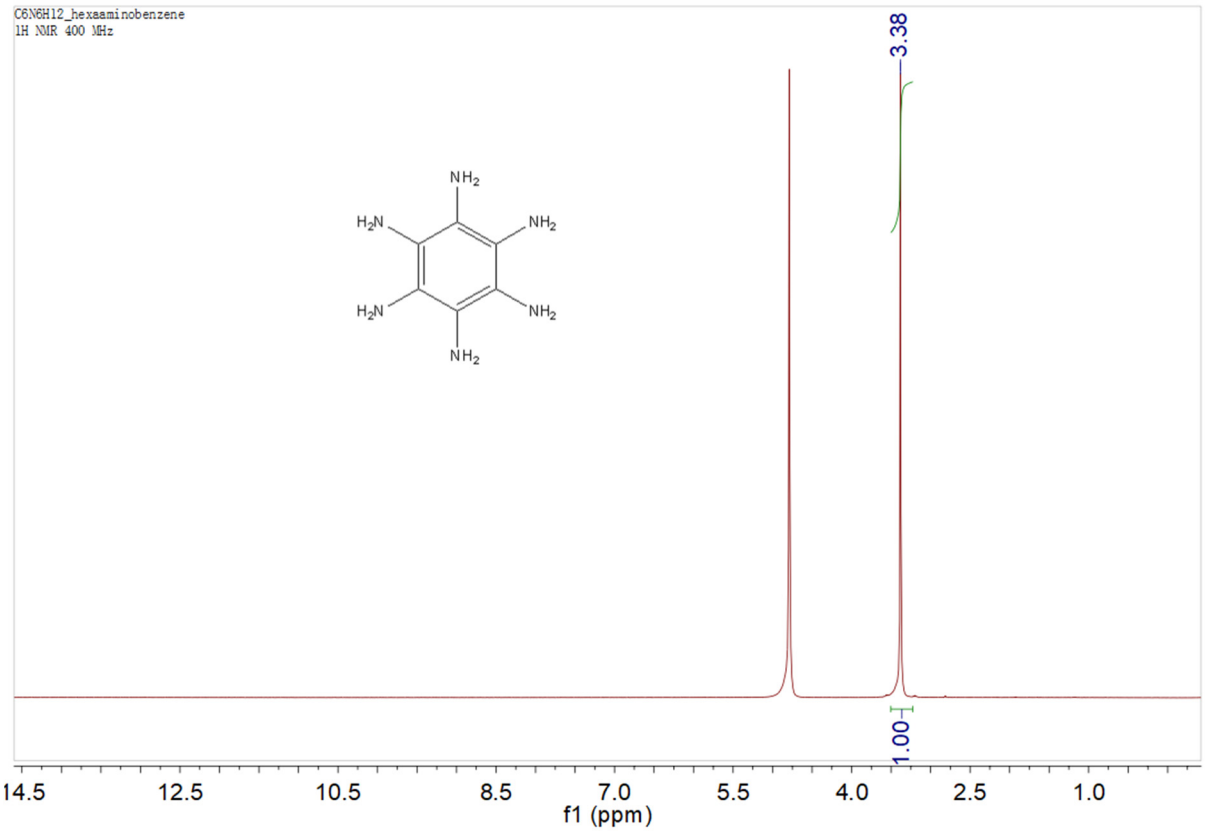

Figure S18. ^{1}H NMR spectrum of hexaaminobenzene

References

[S0] B. Rave, M. Newville, J. Synchrotron Radiat. **2005**, *12*, 537.

[S1]. G, Kresse, J. Furthmüller, *Comp. Mater. Sci*. **1996**, *6*, 15.

[S2]. J. Wu, L. Wang, *J. Mater. Chem*. A **2018**, *6*, 2894-2994.

[S3]. J. Xu, W. Zhang, H. Fan, F. Cheng, D. Su. G. Wang, *Nano Energy* **2018**, *51*, 73-82.

[S4]. https://pubs.acs.org/doi/suppl/10.1021/acscentsci.0c00899

[S5]. https://doi.org/10.1021/acsnano.0c08056

[S6]. X. Song, S. Wang, G. Chen, T. Gao, Y. Bao, L.-X. Ding, H. Wang, *Chem. Eng. J.* **2018**, *333*, 564-571.

[S7]. W. G. Lim, Y. Mun, A. Cho, C. Jo, S. Lee, J. W. Han, J. Lee, *ACS Nano*. **2018**, 12, 6013-6022.

[S8] C. Wang, H. Song, C. Yu, Z. Ullah, Z. Guan, R. Chu, Y. Zhang, L. Zhao, Q. Li, L. Liu, *J. Mater.Chem*. *A* **2020**, *8*, 3421-3430.

[S9] Z. Liu, L. Zhou, Q. Ge, R. Chen, M. Ni, W. Utetiwabo, X. Zhang, W. Yang, *ACS Appl. Mater. Interfaces* **2018**, *23*, 19311–19317.

[S10] J. Li, C. Chen, Y. Chen, Z. Li, W. Xie, X. Zhang, M. Shao, M. Wei, *Adv. Energy Mater*. **2019**, *9*, 1901935.

[S11] Y. Li, J. Fan, J. Zhang, J. Yang, R. Yuan, J. Chang, M. Zheng, Q. Dong, *ACS Nano* **2017**, *11*, 11417-11424.

[S12] Y. Li, J. Wu, B. Zhang, W. Wang, G. Zhang, Z. W. Seh, N. Zhang, J. Sun, L. Huang, J. Jiang, J. Zhou, Y. Sun, *Energy Storage Mate*r. **2020**, 30, 250-259.